LNF - 10/14(P)
April 13, 2010

Technical Design Report of the $\gamma\gamma$ Taggers for the KLOE-2 Experiment

The KLOE-2 Collaboration

G. De Robertis, O. Erriquez, F. Loddo, A. Ranieri,
Dipartimento di Fisica, Università di Bari and INFN sezione di Bari, Bari, Italy

G. Morello, M. Schioppa, S. Stucci,
Dipartimento di Fisica, Università della Calabria and INFN gruppo collegato di Cosenza, Cosenza, Italy

E. Czerwinski, P. Moskal, M. Silarski, J. Zdebik
Institute of Physics, Jagellonian University, Cracow, Poland

D. Babusci, G. Bencivenni, C. Bloise, F. Bossi, P. Campana, G. Capon, P. Ciambrone, E. Danè, E. De Lucia, D. Domenici, G. Felici, S. Giovannella, F. Happacher, E. Iarocci, M. Jacewicz, J. Lee-Franzini, M. Martini, S. Miscetti, L. Quintieri, V. Patera, P. Santangelo, I. Sarra, B. Sciascia, A. Sciubba, G. Venanzoni, R. Versaci
Laboratori Nazionali di Frascati dell' INFN, Frascati, Italy

S. A. Bulychjev, V. V. Kulikov, M. A. Martemianov, M. A. Matsyuk
Institute for Theoretical and Experimental Physics (ITEP), Moscow, Russia

C. Di Donato
Dipartimento di Scienze Fisiche, Università di Napoli "Federico II" and INFN sezione di Napoli, Napoli, Italy

C. Bini, V. Bocci, A. De Santis, G. De Zorzi, A. Di Domenico, S. Fiore, P. Franzini, P. Gauzzi
Dipartimento di Fisica, "Sapienza" Università di Roma and INFN sezione di Roma, Roma, Italy

F. Archilli, D. Badoni, F. Gonnella, R. Messi, D. Moricciani
Dipartimento di Fisica, Università di Roma "Tor Vergata" and INFN sezione di Roma 2, Roma, Italy

P. Branchini, A. Budano, F. Ceradini, B. Di Micco, E. Graziani, F. Nguyen, A. Passeri, C. Taccini, L. Tortora
Dipartimento di Fisica, Università Roma Tre and INFN sezione di Roma Tre, Roma, Italy

B. Hoistad, T. Johansson, A. Kupsc, M. Wolke
Department of Nuclear and Particle Physics, Uppsala University, Uppsala, Sweden

W. Wislicki

A. Soltan Institute for Nuclear Studies, Warsaw, Poland

and

A. Balla, M. Beretta, M. Gatta, L. Iannarelli, C. Milardi, A. Saputi, E. Turri,
Laboratori Nazionali di Frascati dell' INFN, Frascati, Italy

A. Pelosi
INFN sezione di Roma, Roma, Italy

L. Iafolla
Dipartimento di Fisica, Università di Roma "Tor Vergata" and INFN sezione di Roma 2, Roma, Italy

1 Introduction on $\gamma\gamma$ physics

The term "$\gamma\gamma$ physics" (or 'two-photon physics") stands for the study of the reaction (see Fig. 1)

$$e^+e^- \rightarrow e^+e^-\,\gamma^*\gamma^* \rightarrow e^+e^- + X$$

where X is some arbitrary final state allowed by conservations laws.

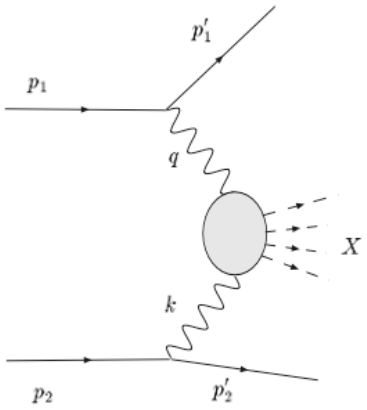

Figure 1: Two-photon particle production in a e^+e^- collider.

Since the two-photons are in a $C = +1$ state and the value $J = 1$ is excluded (Landau-Yang theorem), photon-photon scattering [2] at the e^+e^- colliders gives access to states with $J^{PC} = 0^{\pm+}$, $2^{\pm+}$, not directly coupled to one photon ($J^{PC} = 1^{--}$).

These processes, of $\mathcal{O}(\alpha^4)$, with a cross section of ~ 500 nb, depend on the logarithm of the center of mass energy E, so that, for E greater than a few GeV they dominate hadronic production at e^+e^- colliders.

For quasi-real photons the number of produced events can be estimated from the expression:

$$N \,=\, L_{ee} \int \mathrm{d}W_{\gamma\gamma}\, \frac{\mathrm{d}L}{\mathrm{d}W_{\gamma\gamma}}\, \sigma(\gamma\gamma \rightarrow X) \tag{1}$$

where L_{ee} is the machine luminosity, $W_{\gamma\gamma}$ is the photon-photon center of mass energy ($W_{\gamma\gamma} = M_X$), $\mathrm{d}L/\mathrm{d}W_{\gamma\gamma}$ the photon-photon flux and σ is the cross section into a given final state. By neglecting single powers of $\ln\gamma$ ($\gamma = E/m_e$), when the scattered leptons are undetected in the final state, one has [1]:

$$\frac{\mathrm{d}L}{\mathrm{d}W_{\gamma\gamma}} \,=\, \frac{4}{W_{\gamma\gamma}} \left(\frac{\alpha}{4\pi} \ln\gamma\right)^2 f(z) \qquad z \,=\, \frac{W_{\gamma\gamma}}{2E} \tag{2}$$

with $f(z)$ (Low function) given by

$$f(z) \,=\, \left[(2+z)^2 \ln\frac{1}{z} \,-\, (1-z^2)(3+z^2)\right] \tag{3}$$

The photon flux at $\sqrt{s} = 1.02$ GeV is shown in fig. 2, where accessible final states are also indicated.

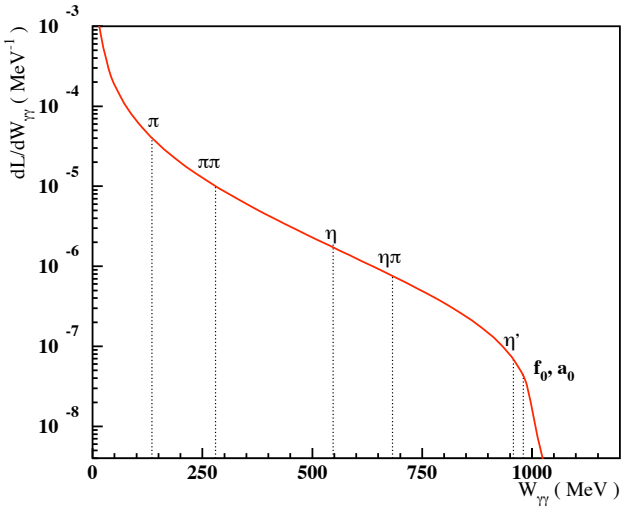

Figure 2: Photon-photon flux at DAΦNE as function of $W_{\gamma\gamma}$ for an integrated luminosity $L_{ee} = 1$ fb^{-1}.

The cross section $\sigma(\gamma\gamma \to X)$ was studied at all of the e^+e^- colliders, from PETRA to CESR to LEP, over the years. In the low-energy region, $m_\pi \leq W_{\gamma\gamma} \leq 700$ MeV, the experimental situation [3] is unsatisfactory for several reasons:

- large statistical and systematic uncertanties due to small data samples and large background contributions;
- very small detection efficiency and particle identification ambiguities for low-mass hadronic systems.

Due to its high luminosity DAΦNE gives the opportunity for precision measurements of low-mass hadronic systems at KLOE-2. A feasibility study for this physics programme was carried out more than ten years ago [4]. In the following we will re-consider some physics topics in the light of the developments since then.

1.1 The process $\gamma\gamma \to \pi^0\pi^0$: the σ case

The existence of the σ meson was suggested for the first time by the linear sigma model to describe pion-nucleon interactions. However, no clear observation of it was provided by the experiments, so that its existence and nature (i.e. quark substructure) is still controversial.

Recently, the situation has changed. It has been shown [5] that the $\pi\pi$ scattering amplitude contains a pole with the quantum numbers of vacuum with a mass of $M_\sigma = 441^{+16}_{-8}$ MeV and a width $\Gamma_\sigma = 544^{+25}_{-18}$ MeV. The σ has been looked for also in D decays by the E791 Collaboration at Fermilab [6]. From the $D \to 3\pi$ Dalitz plot analysis, E791 finds that almost 46% of the width is due to $D \to \sigma\pi$ with $M_\sigma = 478 \pm 23 \pm 17$ MeV and $\Gamma_\sigma = 324 \pm 40 \pm 21$ MeV. BES [7] has looked for the σ in $J/\psi \to \omega\pi^+\pi^-$ giving a mass value of $M_\sigma = 541 \pm 39$ MeV and a width of $\Gamma_\sigma = 252 \pm 42$ MeV.

It is worth to notice that the interest in assessing the existence and nature of the σ meson is not confined to low energy phenomenology. Just to mention a possible relevant physical scenario in which the σ could play a role, consider the contamination of $B \to \sigma\pi$ in $B \to \rho\pi$ decays (possible because of the large σ width). This could affect the isospin analysis for the CKM-α angle extraction [8]. Similarly studies of the γ angle through a Dalitz analysis of neutral D decays need the presence of a σ resonance [9].

In principle, the σ case could be definitively solved by studying the channel $\gamma\gamma \to \pi^0\pi^0$ (i.e the process $e^+e^- \to e^+e^-\pi^0\pi^0$), in the low energy region. (In this energy region $\gamma\gamma \to \pi\pi^-$ is dominated by the Born term due to the photon coupling to the net electric charge of the pions). For this process theoretical predictions exist based on Chiral Perturbation Theory (CHPT) at two-loop level [20] and dispersive techniques [21] (see Fig. 3). Recently, an evaluation of the $\gamma\gamma \to \pi^0\pi^0$ process in presence of the σ resonance has also been performed [10]. The line shape of the cross-section appears to be sensitive to the quark structure of the σ meson, since the two photons directly couple to the electric charge of the constituent quarks.

From the experimental side, the only avalaible data in the energy region of interest come from Crystal Ball collaboration [3][1]. Unfortunately, as show from Fig. 3, these data, affected by large uncertainties, do not allow one to draw any conclusion about the agreement with either of the theoretical approaches, nor on the possible existence of a resonance-like structure in the region around 400-500 MeV.

The effect of the inclusion of the σ resonance, along the line of ref. [10], is shown in Fig. 4. The expected production rates can be calculated by inserting the ChPT prediction for $\sigma(\gamma\gamma \to \pi^0\pi^0)$ in eq. (1). In this case the integral runs over the region $W_{\gamma\gamma} = [2m_\pi, 2E]$, i.e. beyond the validity domain of ChPT ($W_{\gamma\gamma} \leq 700$ MeV). We choose a conservative extrapolation for the cross section in the region $W_{\gamma\gamma} > 700$ MeV corresponding to the value given by ChPT for $W_{\gamma\gamma} = 700$ MeV, and:

$$\sigma(e^+e^- \to e^+e^-\,\pi^0\pi^0) \;\simeq\; 13\ \mathrm{pb}\,, \tag{4}$$

i.e. 13,000 events for an integrated machine luminosity of 1 fb^{-1}.

1.2 Pseudoscalar mesons in $\gamma\gamma$ processes

Since the radiative width of pseudoscalar mesons is small, the only way to measure it is to study the meson formation in $\gamma\gamma$ reactions.

The $e^+e^- \to e^+e^-X$ processes, with $X = \pi^0, \eta, \eta'$, has a cross section that can be evaluated

[1] In this energy region there are also unnormalized JADE data [19]. Upon arbitrary scaling they are consistent with Crystal Ball data.

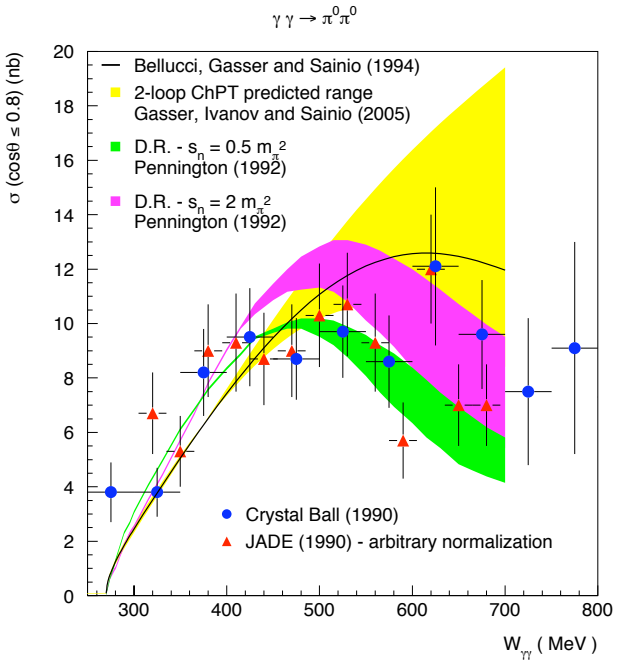

Figure 3: Comparison of all the present data from Crystall Ball and JADE (arbitrarely normalized at the Crystall Ball data) to the predicitions from ChPT (solid and yellow band) and dispersion relation techniques (green and magenta bands).

using the narrow width [11] approximation:

$$\sigma(e^+e^- \rightarrow e^+e^-X) = (4\alpha \ln\gamma)^2 \, f(z) \, \frac{\Gamma_{X\gamma\gamma}}{m_X^3}$$

with $z = m_X/2E$, where m_X is the meson mass and $\Gamma_{X\gamma\gamma}$ is the partial width for $X \rightarrow \gamma\gamma$.

Table 1: Values for the $\sigma(e^+e^- \rightarrow e^+e^-X)$ (pb) process at 510 MeV beam energy.

π^0	η	η'
271	45	4.9

The $\Gamma_{X\gamma\gamma}$ measurements are a crucial input for:

- the determination of the pseudoscalar mixing angle φ_P, where we have [12]:

$$\frac{\Gamma(\eta \rightarrow \gamma\gamma)}{\Gamma(\pi^0 \rightarrow \gamma\gamma)} = \left(\frac{m_\eta}{m_{\pi^0}}\right)^3 \frac{1}{9} \left(5\cos\varphi_P - \sqrt{2}\frac{\bar{m}}{m_s}\sin\varphi_P\right)^2$$
$$\frac{\Gamma(\eta' \rightarrow \gamma\gamma)}{\Gamma(\pi^0 \rightarrow \gamma\gamma)} = \left(\frac{m'_\eta}{m_{\pi^0}}\right)^3 \frac{1}{9} \left(5\sin\varphi_P + \sqrt{2}\frac{\bar{m}}{m_s}\cos\varphi_P\right)^2$$

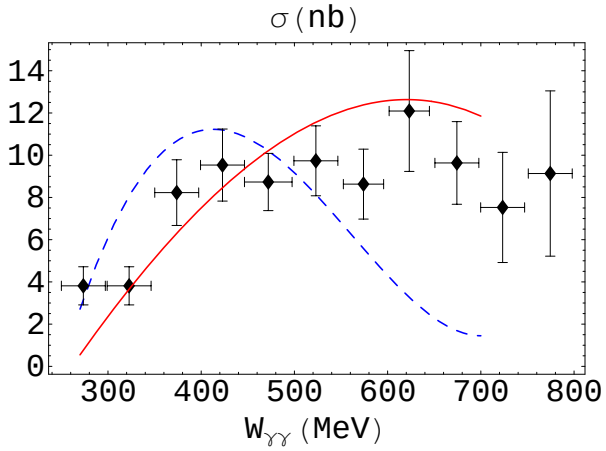

Figure 4: The Crystall Ball data and the two-loop ChPT prediction (red curve) of Fig. 3 are compared with the the cross section for the process $\gamma\gamma \to \sigma \to \pi^0\pi^0$ calculated in ref. [10] (blu curve).

- the test for valence gluon content in the η' wavefunction [13, 14]:

$$\frac{\Gamma(\eta' \to \gamma\gamma)}{\Gamma(\pi^0 \to \gamma\gamma)} = \left(\frac{m'_\eta}{m_{\pi^0}}\right)^3 \frac{1}{9} \cos^2\phi_G \left(5 \sin\varphi_P + \sqrt{2}\frac{f_n}{f_s}\cos\varphi_P\right)^2$$

Furthermore, a precise study of the form factors [15] of the transition $\gamma\gamma^* \to X$, $F(Q^2_{\gamma^*}, 0) = F(Q^2_{\gamma^*})$, where one photon is off-shell and the other is real, allows one to test:

- phenomenological models used for computing the light-by-light contributions to the $(g_\mu - 2)/2$ prediction in the Standard Model [16];
- the dynamics of the $\pi^0 \to e^+e^-$ transition [18], whose branching fraction value was recently measured by the KTeV experiment [17] and is apparently larger than the unitarity bound derived from $\pi^0 \to \gamma\gamma$.

2 Experimental considerations

In the following we will focus our attention on the measurement of $\gamma\gamma \to \pi^0\pi^0$. To improve on the measurement of the $\gamma\gamma \to \pi^0\pi^0$ cross section, high statistics has to be complemented by a careful control of the systematics which cannot be obtained without strong reduction of background events. The main source of background comes from ϕ decays. Studies currently underway on the KLOE data sample are using the off-peak data in order to evaluate the experimental capabilities leaving aside most of the background from ϕ decays. At KLOE-2 we aim to analyze the on-peak sample performing background suppression with the information coming from a tagger system for efficient detection of scattered electrons. Then, on the tagged sample, we can use the kinematical constraint on the total transverse momentum (p_T) of the particles in KLOE to further suppress the events from e^+e^- annihilation, that have higher p_T with respect to $\gamma\gamma$ ones. It is worthwhile to mention that tagging the two-photon events would also be useful to reject a possible background for particular measurements of one-photon processes, like the measurement of the $e^+e^- \to \pi^+\pi^-$ cross section from Initial State Radiation events.

From the study of the kinematics of the reaction $e^+e^- \to e^+e^-\pi\pi$ the most of the scattered electrons are emitted in the forward directions, escaping detection. Since the energy of these electrons is less than 510 MeV, they deviate from the equilibrium orbit during their propagation along the machine lattice. Therefore a tagging system should consists of one or more detectors located in well identified regions along the beam line, aimed at determining the energy of the scattered electrons either directly, or from the measurement of their displacement from the main orbit.

To fix the characteristics of the tagging detectors and their location along the machine layout we made a complete study of the tracking of the final leptons in the process $e^+e^- \to e^+e^-\pi^0\pi^0$ along the machine optics.

2.1 Tracking of the off-energy leptons in the machine lattice

In order to properly locate the $\gamma\gamma$ taggers in DAΦNE, we need to accurately track the off-energy particles along the machine optics. In particular, the region of the DAΦNE collider for estimating the particles path starts at the interaction Point (IP) and ends at the exit of the first bending dipole at the end of the straight section. In Fig. (5) we show the magnetic layout of the transfer line of the DAΦNE collider relevant for taggers. Of the two lines shown in the figure, the lower one is the positron short line, used for the simulations.

The code generally used for optics calculations in accelerator physics is Mad [23]. This code is strictly thought to study the optical properties of the nominal beam (the one for which the magnetic elements are set). The error in the tracking of off-momentum particles comes from the approximate methods used for these particles through the magnetic elements, set for nominal design momentum. This error becomes more and more important as much as the particle energy deviate from the nominal one. For our study, however, we need a tool that allows us to calculate the nominal and the off-energy particle tracks with the same precision, while using the magnetic element coefficients extracted from the Mad model. This determines the choice of using the `BDSIM` [24] code. In `BDSIM`, particle tracks are calculated by solving the equation of motion, taking into account the Lorentz force in presence of a magnetic field. A

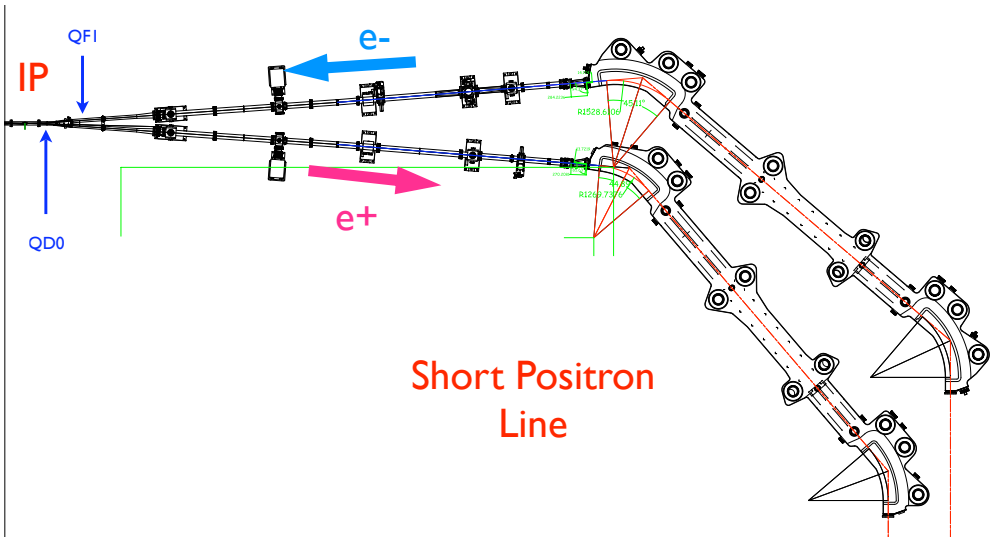

Figure 5: Magnetic layout of one side of DAΦNE Main Rings relevant for the $\gamma\gamma$ tagger.

more detailed description of Bdsim structure and functionality can be found in reference [25].

We have firstly calculated the path of a nominal particle, a positron of 510 MeV energy, to check that it fits exactly with the QF1 line[2]. This check is needed to demostrate that the transfer line has been correctly modelized (corrected values of the QD0 quadrupole coefficient and the center of all the magnetic elements). In Fig. (6) the blue line in the middle of the beam-pipe represents the nominal trajectory. The (x, y, z) coordinates calculated with Bdsim, have been superimposed on the technical design of the beam-pipe boundary, to check that the nominal particle track is actually centered on the related transfer-line.

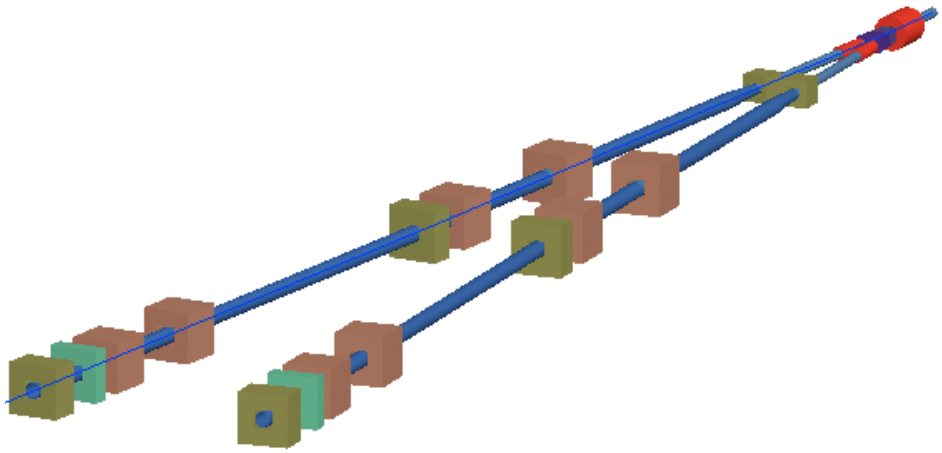

Figure 6: Nominal trajectory in Bdsim model.

As second step, we calculated the trajectories of all particles with energy from 5 MeV up to

[2]We define the QF1 line the part of transfer line on which QF1 is mounted. This is rotated of about 4 degree with respect to the absolute z axis (coincident with the QD0 axis)

510 MeV in steps of 0.5 MeV. All these particles have been produced at the IP with the same direction of the nominal one (-25 mrad with respect of the z axis).

The results of the simulations have been summarized in the Tab. 2, in which we report the z-coordinate along the beam transfer line for particles of different energy.

Energy Range[MeV]	Distance fro IP[cm]	description
0-150	0-53	from IP to end of QD0
155-220	53-79	inside the splitter
225-255	79-84	inside QF1
260-325	from 340-760	between quaps100-quaps102

Table 2: Sketch of the zones where off-momentum particles are lost along the line in absence of solenoidal field (the results refer to particles of all energy but starting at IP with -25 mrad).

The particles with energy lower than 260 MeV impinge on the internal side (with respect to the central point of the machine) of the beam pipe (see Fig. (7)). On the contrary, particles with energy in the 260-330 MeV range impinge on the external side of the beam-pipe (see Fig. (8)). Finally, the trajectories followed by particles arriving at the entrance of the bending magnet are sketched in Fig. (9).

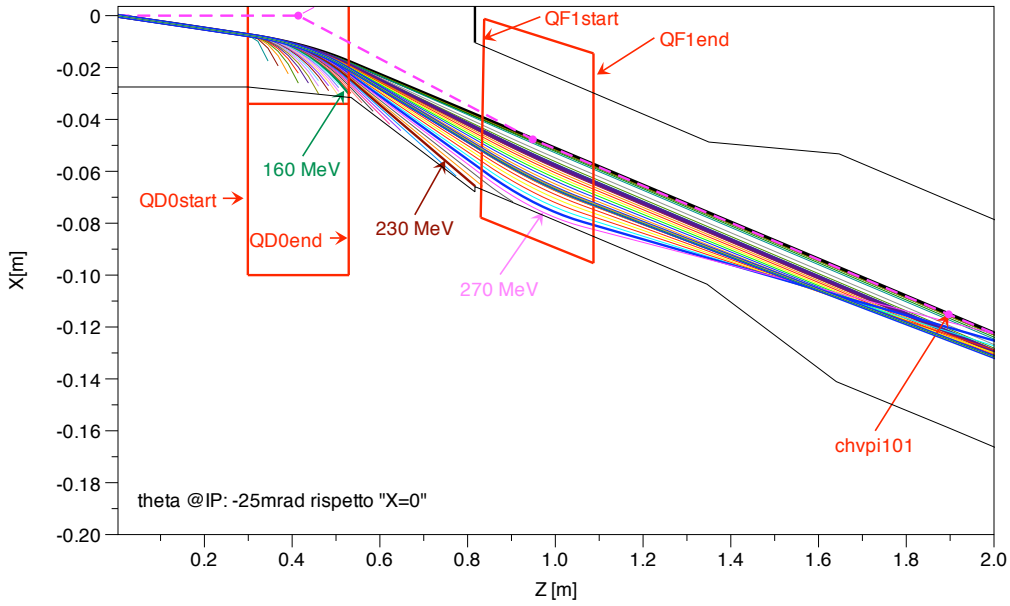

Figure 7: Sketch of the trajectories of all particles up to 2m away from IP.

The effect of the emission angle of the particles at the IP has also been taken into account [26].

The modeling of the dipole in Bdsim has required a lot of work, both for the complex geometry of this component and for the fact that Bdsim has been essentially developed to work for linear machines. The main difficulty comes from the positioning of markers inside the dipole (needed for collecting the information to reconstruct the trajectories), due to the fact that the

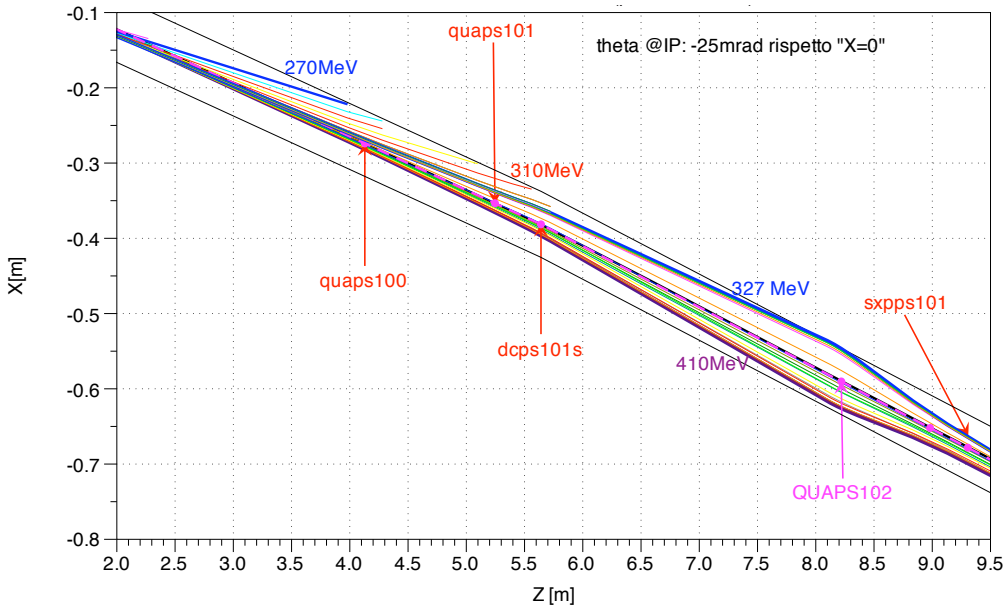

Figure 8: Sketch of the trajectories of particles with energy ranging between 270 MeV and 510 MeV.

standard plane markers are to be perpendicular to the z-axis, while the main geometrical axis of the pipe inside the dipole rotates of 40.5 degrees. Two strategies have been followed to realize the dipole model: the first one used the standard options of Bdsim, the second one defining new marker elements resulting in a modified version of the code. The results from the two models are in perfect agreement and this successful comparison allowed us to validate the simulations. In Fig. (10) one of the two models used in Bdsim has been shown. The trajectories of the particles emerging from the dipole are sketched in Fig. (11).

The results discussed so far have been obtained in absence of the magnetic field of the KLOE detector. Actually, the detector operates with a magnetic field of nominal central value equal to 0.52 T and the z-profile reported in Fig. (12).

The analysis of the trajectory modification due to the KLOE magnetic field has required to redefine the Bdsim model in a way to introduce properly the magnetic global component B_z in all the elements inside the KLOE region (about 2 m from the IP). As first step of the analysis, a validation of the modified Bdsim model has been successfully performed, comparing the track of the nominal particle with the corresponding one estimated by the Mad code. This comparison (shown in Fig. (13)) has been performed in the region from the IP up to the QF1 outlet without the insertion of the new permanent dipole correctors, which have to be placed just after QF1.

As we can see in Fig. (13), the nominal tracks calculated by Bdsim and by Mad agree perfectly. This makes us confident in having properly inserted the solenoidal field in Bdsim. In Fig. (14) it is reported a 3-dimensional view of the 510 MeV trajectory in a range of 1m apart from IP. The maximum displacement at the end of QF1 is about 3.5 mm in the vertical direction.

Subsequently, the modifications of all the trajectories coming out in the region between

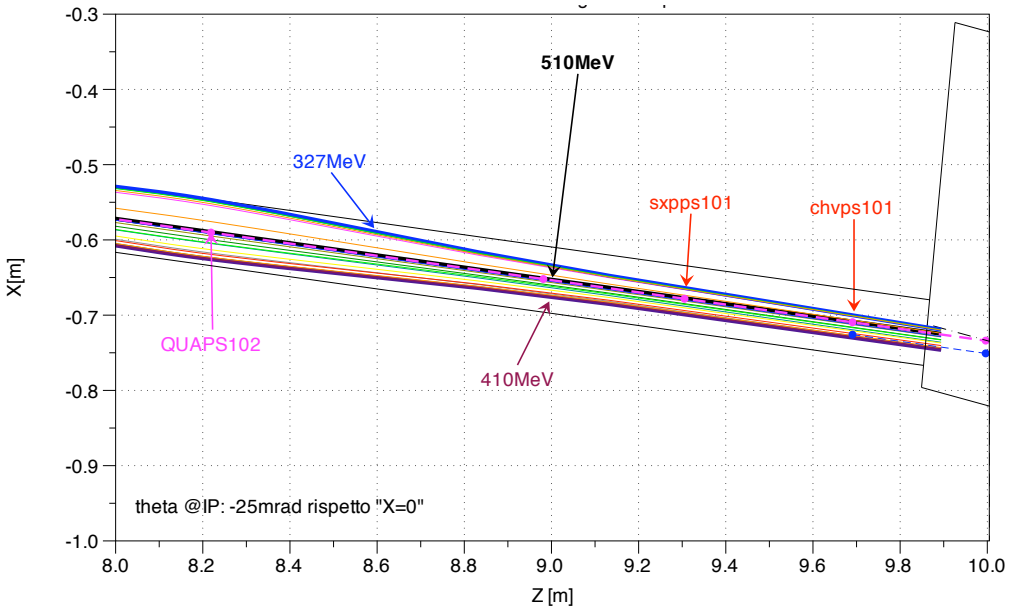

Figure 9: Sketch of the trajectories of particles arriving at the dipole.

QD0 and QF1 have been estimated and compared with the ones in absence of KLOE field. The effect of the solenoidal field on the tracks is to decrease (6 cm for the particle with energy 220 MeV) the global absolute z-coordinate where the particles are lost, while for the x-coordinate the effect is of the order of mm.

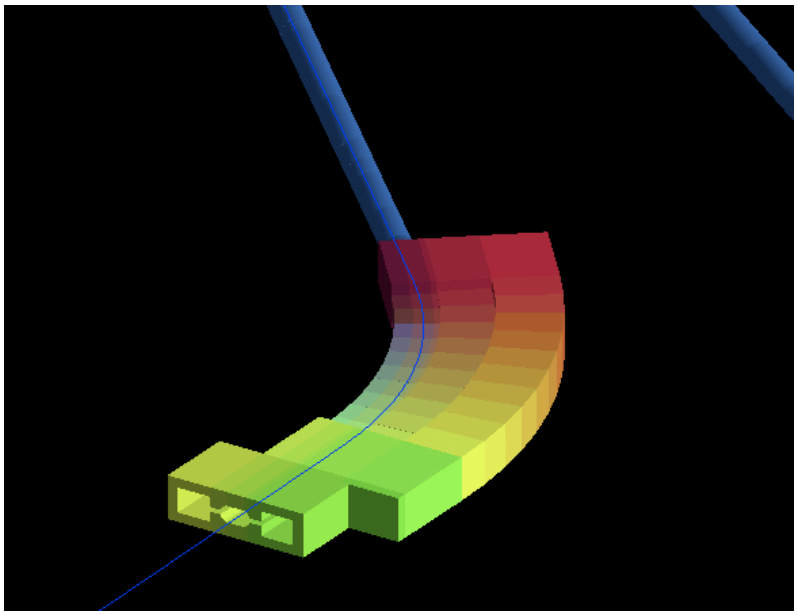

Figure 10: Bdsim model of the dipole at the end of the straight section. The blu line is the nominal track.

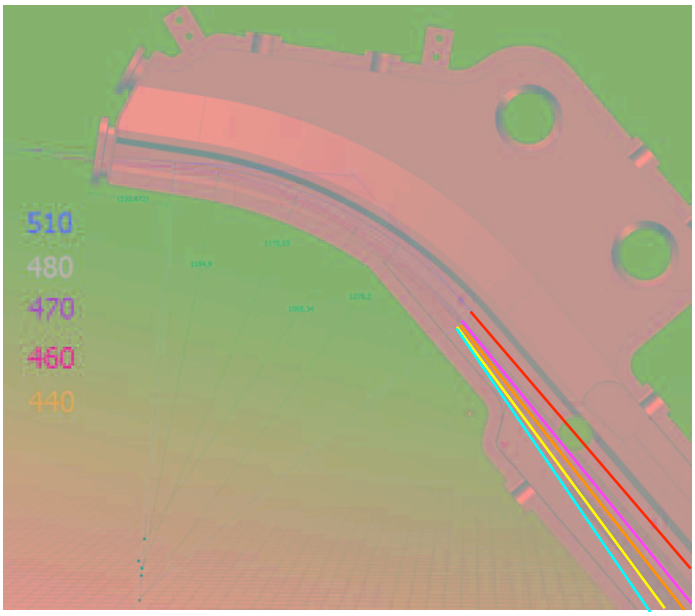

Figure 11: Off-momentum particles surviving after the dipole ($E \geq 430$MeV).

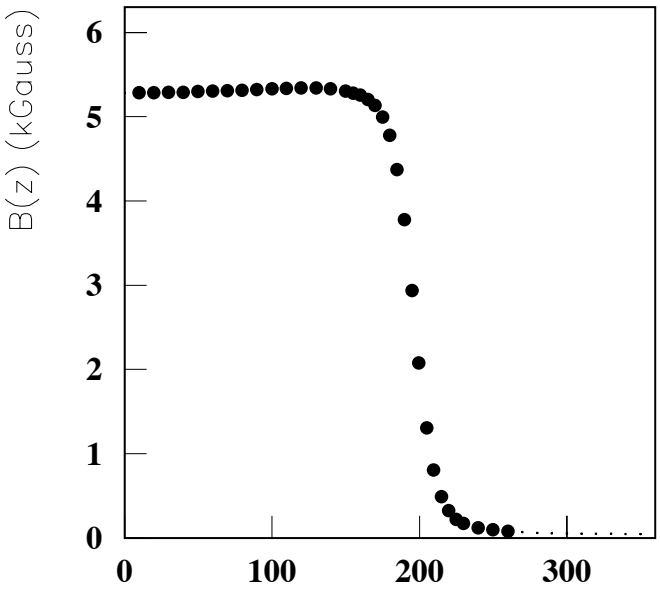

Figure 12: Magnetic field of Kloe

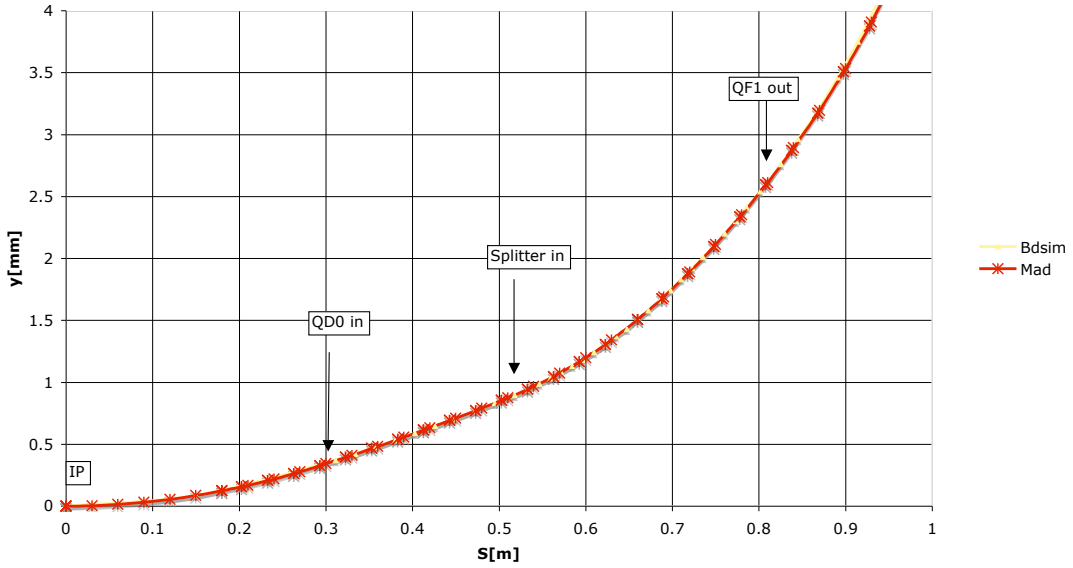

Figure 13: Comparison between Mad and Bdsim. Vertical displacement of the nominal trajectory (510 MeV) due to KLOE field.

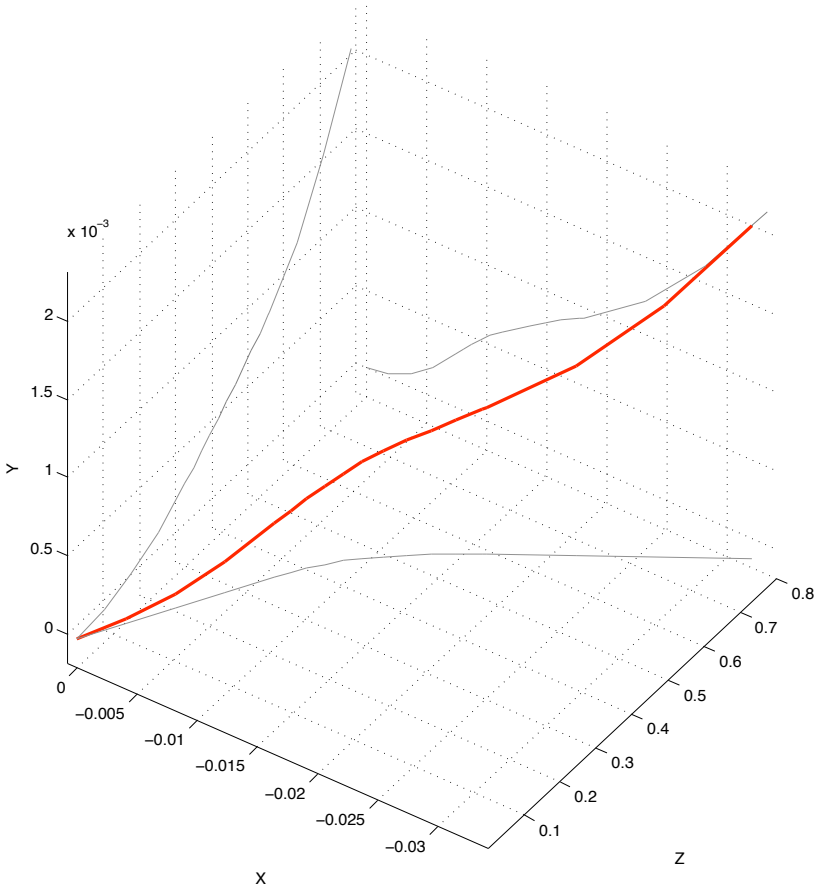

Figure 14: 3D view of nominal trajectory before entering QF1 in presence of the solenoidal KLOE field. The origin of the frame coincides with the IP.

2.2 The generator for $e^+e^- \to e^+e^-\pi^0\pi^0$

We have considered two different generators for the process $e^+e^- \to e^+e^-\pi^0\pi^0$:

- The MC code developed by Courau [22] based on the Double Equivalent Photon Approximation (DEPA), i.e. the photons emitted by the incoming leptons are considered nearly on-shell. Therefore, this code cannot properly describe the case in which the final leptons are emitted at large angles with respect to the incoming ones. On the other hand, it is fast, thus allowing generation of events in any invariant mass range.

- The code developed by Nguyen et al. [10]. Here the σ meson is explicitely inserted as a Breit-Wigner function with mass and width taken from E791 data. This code was tuned for events generated 20 MeV below the ϕ resonance peak, i.e. for sqrt(s) = 1 GeV.

In addtion we have checked the results of the two generators above, with what obtained by using TREPS [27]. This code, developed by the Belle Collaboration, has been modified by the author to run it in the region of our interest, assuming a uniform cross section for the process $\gamma\gamma \to \pi^0\pi^0$. A comparison among the results obtained by the use of these three codes is shown in figs. 15, 16 and 17.

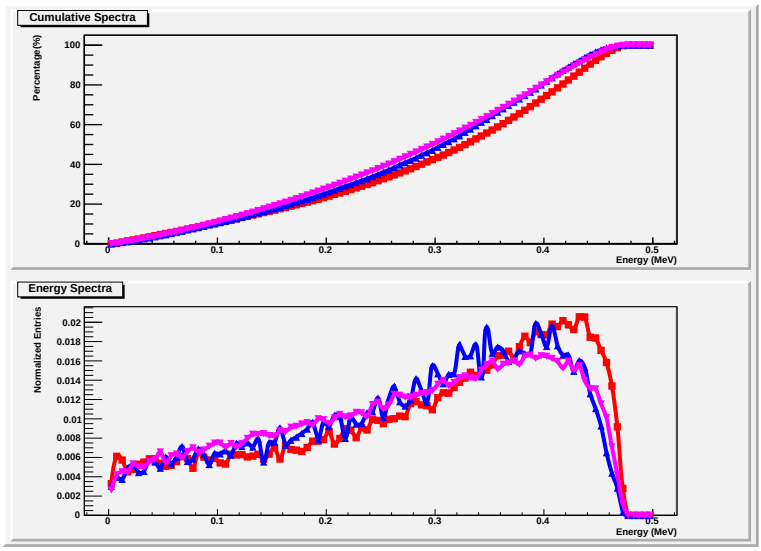

Figure 15: Comparison among the energy distribution for the final leptons produced by the three generators under consideration: Courau (red), Nguyen et al. (blu) and TREPS (purple).

The energy distribution generated with TREPS is in agreement with the one generated with Nguyen et al. code. The difference with the Courau code is more evident, even if the maximum energy is almost the same. As for the angular distributions the difference among the three codes is concentrated around the first point (1 degree). The maximum value of the absolute difference is below 5 %.

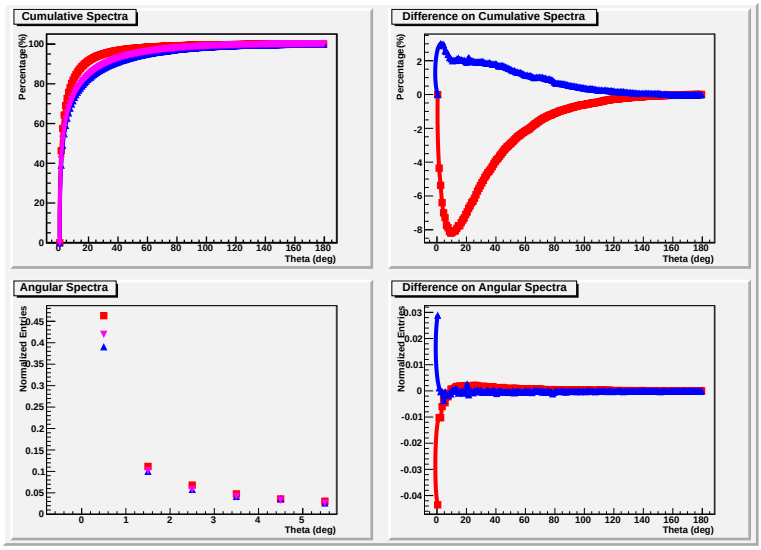

Figure 16: The same of Fig. 15 for the angular distribution of the final leptons.

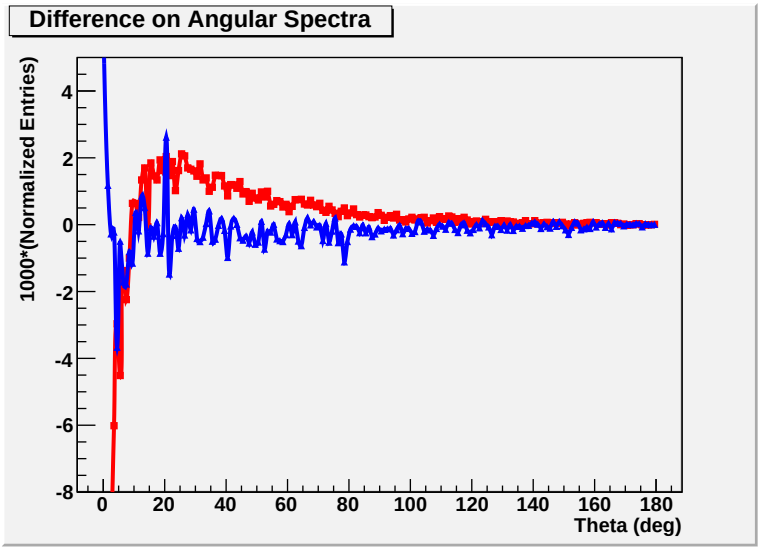

Figure 17: Zoom of lower-right panel of Fig. 16 for $\theta > 1^o$.

3 The tagging system

The results of the study described in the previous sections show that, despite the constraints due to the DAΦNElayout, a good coverage of the kinematic region of interest can be achieved. Satisfactory results can be obtained by the use of a tagging system composed by two stations located at $\sim$ 1 m and $\sim$ 11 m from the interaction region, respectively:

- A station to detect leptons at low energy (LET), located in the region between the two quadrupoles inside KLOE (QD0 and QF1). According to the tracking, the energy of the scattered leptons arriving on this detector is in the interval (160 $\div$ 230) MeV.
- A station for leptons with high energy (HET), located at the exit of the first bending magnet (about 11 m from the IP). The energy of the scattered particles is in this case (425-490) MeV. The upper limit of the interval is determined by the minimum distance (3 cm) from the main orbit where we can place the detector without interfere with proper DAΦNE operations.

Leptons of energy not comprised in the ranges of the LET and the HET can in principle be detected by a third station (MET) located somewhat in between the other two. This possibility is however not taken into consideration by the present study, leaving a complete study of the MET for a future note.

3.1 The LET detectors

The only magnetic element seen by the scattered leptons that reach the LET is QD0. They are deflected, with respect to the nominal beam orbit, because their energy is lower than 510 MeV and because they are off-axis with respect to QD0. Therefore, their energy distibution is broad ranging between 50 and 450 MeV. This is shown in Fig. 18 where we compare the energy distribution for different regions of the z-coordinate of the impact point on the beam pipe comprised between the exit of QD0 and the entrance of QF1s. For the above reason a measurement of their impact point is not useful to determine their energy, which has to be determined calorimetrically. According to the simulation the fraction of all leptons generated at IP reaching this detector is 17 %.

In Fig. 19 we show the correlation between the energy and angle of the final leptons (we remind the reader that the incoming beam is inclined by -25 mrad with respect to the machine axes).

3.2 The HET detectors

This detectors are located 11 m away from the IP. This means that the final state leptons propagate along several different magnetic elements of the machine before reaching them. As a consequence of that, the beam pipe acts as a sort of "angular filter". This is clearly shown in Fig. 20, where we compare the angular distribution of the leptons reaching the HET with respect to one generated at the IP. Only the leptons emitted inside a cone of aperture of $\Delta\theta < 40$ mrad around the flight direction of the incoming beam are detected. For this reason, we can make use of a position detector. Since we deal with leptons that have lost a small amount of

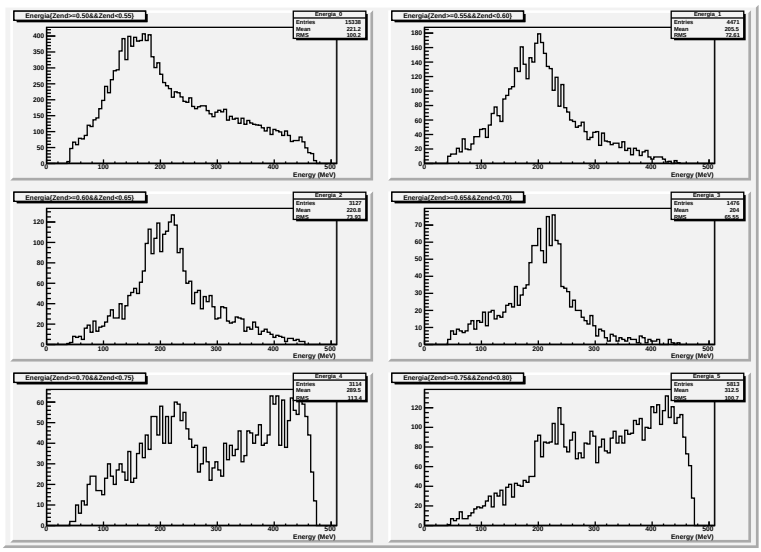

Figure 18: Energy distribution of the final leptons impinging on LET detector for different intervals of the z-coordinate of the impact point.

their initial energy, this function is linear. This plot also shows that a detector 15 cm wide will tag leptons with energy comprised between 430 and 475 MeV, with the upper limit fixed by the considered reaction. In the linear fit the parameter $p_0 = 506.6 \pm 0.5$ MeV is the energy associated to the main orbit while the parameter $p_1 = -0.5645 \pm 0.0059$ MeV/mm corresponds to the energy resolution of the detector. We have also studied the impact of possible variations of the beam conditions on the determination of these parameters. We have considered variations of the coordinate (x, y) of the IP and the emission angle of the final lepton with respect to the direction of the incoming beams. We have considered 15 different regions of these variables and for each region we have studied the linear relation between the displacement with respect to the main orbit and the energy of final leptons. In figure 22 we show the distributions for the parameters $p_{0,1}$. The parameter p_0 changes to $p_0^{fin} = 507.7 \pm 1.1$ MeV, while the angular coefficient of the straight line becomes $p_1^{fin} = -0.5854 \pm 0.0110$ mm/MeV.

This means that the energy calibration of the HET detector is largely insensitive to the nature of the specific process producing the final leptons. Furthermore, according to the simulation, the fraction of all leptons generated at IP reaching this detector is 14 %.

3.3 Correlations between tagging stations

By the knowledge of the lepton energy $E'_{1,2}$ of the particles impinging on each detector, it is possible to compute the region of photon-photon invariant mass covered by the correlation between each possible pair of tagging detectors. By assuming that each photon is emitted along the flight direction of the corresponding lepton, one has:

$$\sqrt{W_{\gamma\gamma}^2 - 4m_e^2} \simeq 2\sqrt{\omega_1\omega_2}\cos\theta\,, \tag{5}$$

where we have estimated as $2m_e^2$ the squared "masses" of the virtual photon. In equation (5) θ is the angle (± 25 mrad) between each beam and the geometrical axes of the machine and

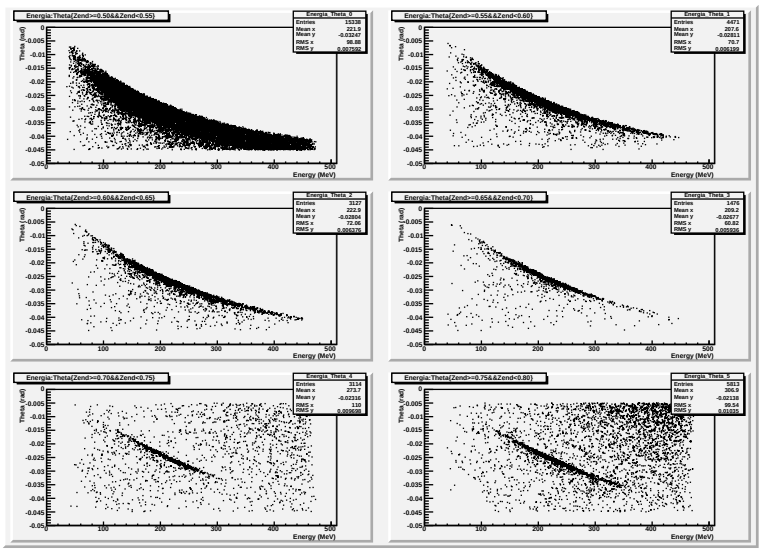

Figure 19: Angle vs Energy correlation of the leptons impinging on LET detector. The intervals of z-coordinate of the impact point are the same of Fig. 18.

$\omega_{1,2} = E - E'_{1,2}$ are the energies of the two photons, respectively. More generally, the photons are emitted at angle with respect to the leptons flight direction. This translates in an effective θ to be inserted in equation (5). This angle can be evaluted by using the Courau generator, and turns out $\langle\theta\rangle = 69.5 \pm 51.7$ mrad. Eq. (5) specified for this angle provide us the $W_{\gamma\gamma}^{meas}$. By indicating with $W_{\gamma\gamma}^{sim}$ the photon-photon invariant mass simulated by the generator, in Fig. 23 we show the difference between the $W_{\gamma\gamma}^{sim} - W_{\gamma\gamma}^{meas}$ in the ideal case where the HET/LET detector resolution is infinite, and in a more realistic case where we assume the HET resolution to be $2p_1^{fin}$, i.e. a 2 mm pitch is considered, and LET resolution is $\sigma(E)/E = 5\%/\sqrt{E[Gev]}$. In the case of the HET $\otimes$ LET coincidence we have a resolution of σ_E =8.2 MeV, while in case of the LET $\otimes$ LET coincidence we have a resolution of $\sigma_E = 47$ MeV.

In figure 24 the invariant mass coverage for the two coincidence HET $\otimes$ LET and LET $\otimes$ LET is showed where is clearly indicated that we cover the $W_{\gamma\gamma}$ from threshold up to 700 MeV.

3.4 Considerations on backgrounds

Backgrounds, generated by Touschek effect or radiative Bhabha are a major concern for the proper operation of both HET and LET. We have tried to estimate the amount of the DAΦNE background experimentally, during the run of the SIDDHARTA experiment in July 2008. For the purpose we have used a prototype of the GRAAL tagging system, consisting of a silicon μstrip 1 mm thick, with 300 μm pitch backed by five $5 \times 5 \times 6$ mm^3 Bicron BC418 plastic scintillators located very close the LET position. Another plastic scintillator was located after the dipole, close to the HET position but outside the beam pipe which provides a natural shielding to the detector. In Fig. (25) we report the counting rate of the plastics detectors in the two location studied during a typical DAΦNE run. The corresponding average luminosity is around 10^{32} cm^{-2}s^{-1}. The measured average background is about 200 kHz in the LET location and 100 kHz in the HET one. These numbers have to intended just as a qualitative estimate

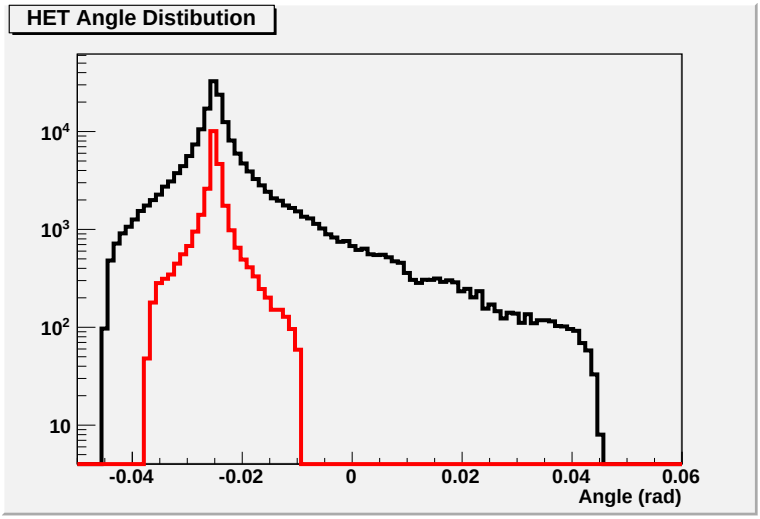

Figure 20: Angular distribution of the leptons impinging HET detector (red) respect to the one of all generated leptons (blalck).

of the real background that will affect our tagging detector. We remark that for the LET the mesurated rates taking into account both the two backgroud sources, Touschek and radiative Bhabha, while for the HET the beam pipe shielding reduce the background rates measured.

3.5 Radiative Bhabha Scattering

The radiative Bhabha scattering ($e^+e^- \rightarrow e^+e^-\gamma$) has been simulated using the `BHABHAYAGA` code. We have generated 100000 events imposing the following kinematical constraints:

- minimum photon energy equal 10 MeV;
- minimun final lepton energy 50 MeV;
- emission angle of the final leptons comprised between 870 μrad and $\pi-870$ μrad respect to the direction of the incoming leptons.

The corresponding cross section turn out to be 12.7 mb. By using `BDSIM` code, the final leptons are then trackend along the machine optics. The acceptance for the LET and HET detectors turn out to be 6 % and 17 %, respectively. By assuming a DAΦNE luminosity of $5 \times 10^{32}\ cm^{-2}s^{-1}$, this implies total rates of about 400 kHz for the LET and 1.1 MHz for the HET.

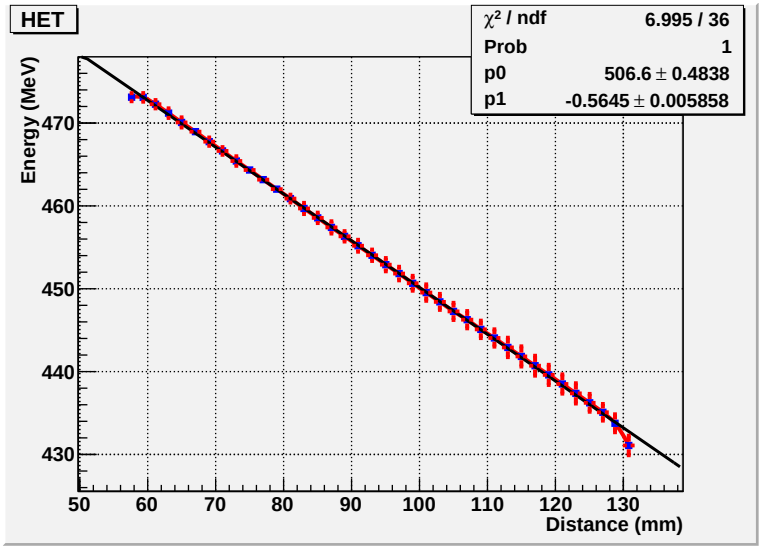

Figure 21: Energy of the leptons arriving on the HET against their displacement from the main orbit.

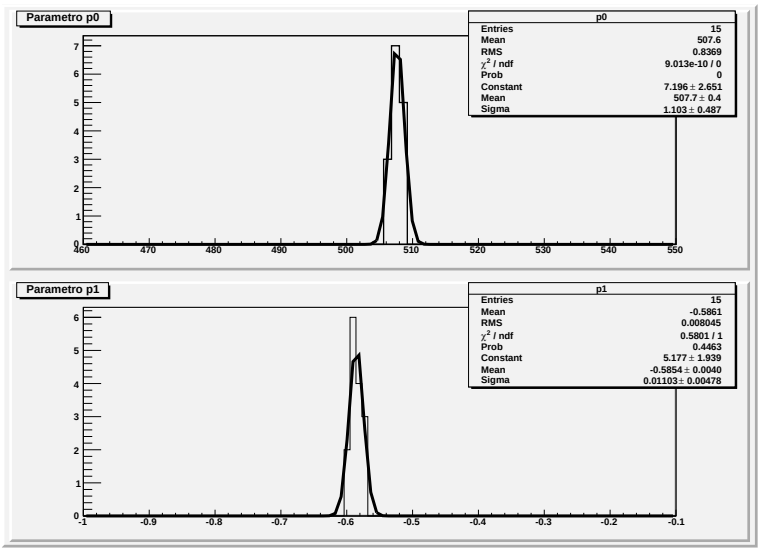

Figure 22: Influence of the initial condition on the parameter p_0 and p_1

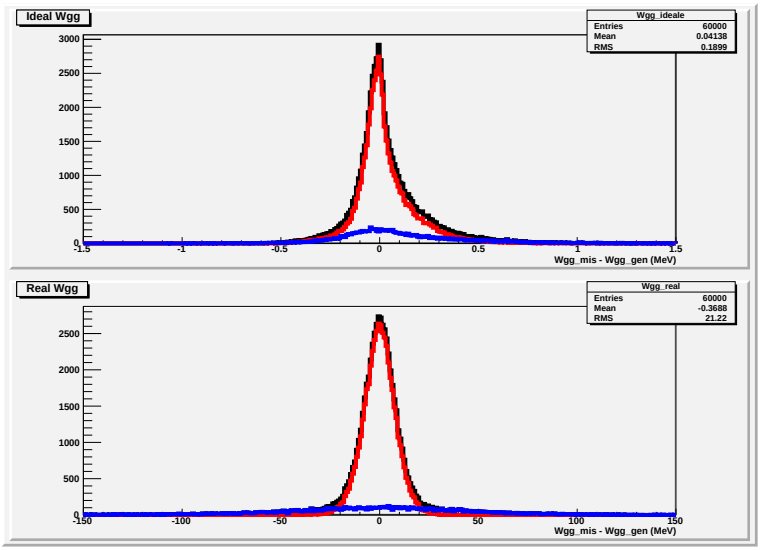

Figure 23: Distribution for the variable $W_{\gamma\gamma}^{sim} - W_{\gamma\gamma}^{meas}$ for ideal (upper panel) and realistic (lower panel) detectors (see text). The red curve corresponds to HET $\otimes$ LET coincidence, while the blue one corresponds to the LET $\otimes$ LET coincidence.

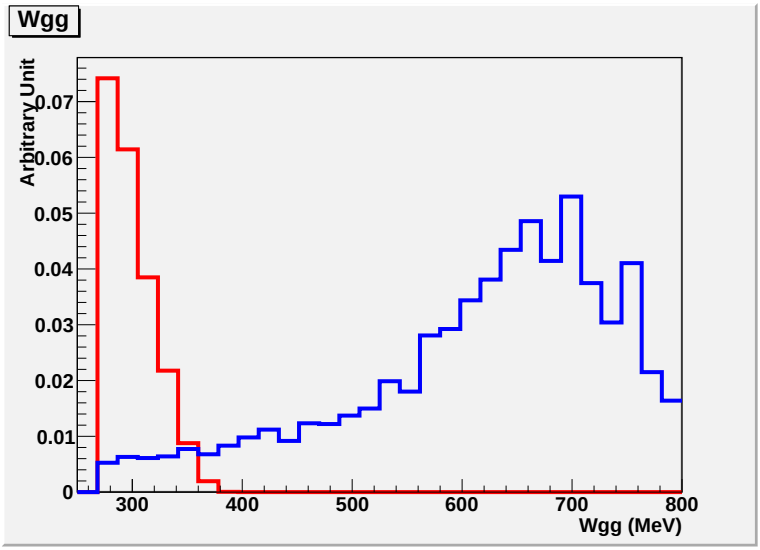

Figure 24: Acceptance coverage, Eff, as function of the $W_{\gamma\gamma}$(MeV) for the HET $\otimes$ LET (red curve) coincidence and LET $\otimes$ LET coincidence (blue curve).

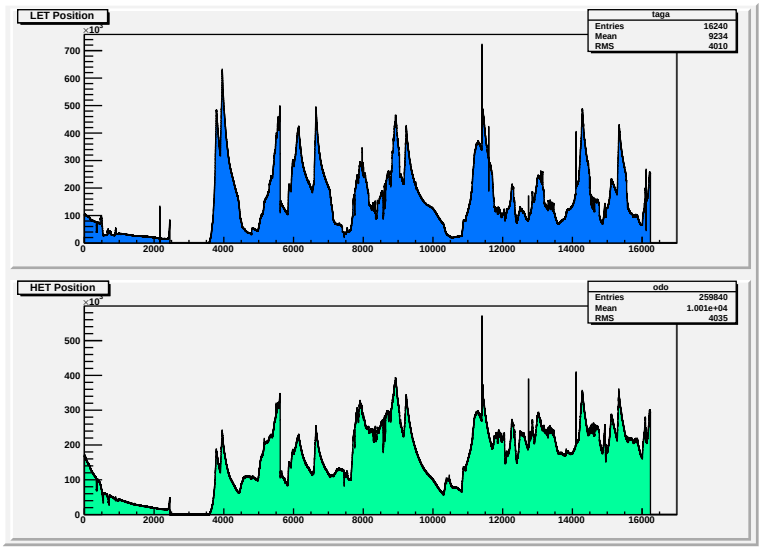

Figure 25: Counting rate behaviour during a run period of six hours

4 LET detector design

In the previous chapters the results of the beam simulation were discussed: the knowledge of expected direction of the off-energy beam particles allows us to evaluate, as a function of the particle momentum, where the off-energy electrons and positrons will hit the beam pipe wall. The simulation shows that low energy e^+e^- , i.e. the ones with energy below 250 MeV, come out from the beam pipe within one meter from the interaction point. These particles can be identified by a detector very close to the beam pipe, placed in the horizontal plane. However, off-energy e^+e^- detectable in this way are only those crossing the beam pipe in a region where no magnetic element is present, i.e. where it is possible to place a detector. The only free region in the zone of interest is the one sitting between the first two quadrupoles close to the IP. There, most of the off-energy e^+e^- coming out the beam pipe have energy between 160 and 230 MeV and an average angle of 11 degrees with respect to the beam axis. The cross section of the emitted beam will be 3 cm along the horizontal axis, with negligible vertical spread. The latter dimension is mainly due to the effect of the KLOE magnetic field, which is parallel to the beam axis and deflects off-beam particles in the vertical plane.

The simulation also shows that for these off-energy e^+e^- there is only a rough correlation between particle energy and trajectory, due to the spread of the interaction point and orbit, allowing off-momentum e^+e^- with energies within few tenth of MeV to pass through the beam pipe wall at the same point. This loss of correlation between energy and position makes it necessary to design an energy-sensitive detector, i.e. a calorimeter, instead of a position-sensitive one.

A further costraint to be considered is the presence of the KLOE drift chamber inner wall: this limits the radial dimension of the detector below 20 cm, when accounting also for the clearance necessary to install the inner detectors and the beam pipe.

The inner station of the $\gamma\gamma$ tagger will therefore consist of a couple of detectors, symmetrically placed at both sides of the interaction point, in a position which allows us to detect the escaping beam particles. This inner detector, referred as Low Energy Tagger or LET, consists of a calorimeter capable of detecting electrons and positrons in the energy range 160-230 MeV. The environmental conditions require radiation-tolerant devices, insensitive to magnetic fields. Concerning the physics requirements, such a detector must allow for high energy and time resolutions:

- Energy resolution is required to improve the reconstruction of the invariant mass of the $\gamma\gamma$ decay products, both in case of HET-LET and LET-LET event tagging.
- Time resolution is required to correctely correlate the detected events with the bunch crossing that has generated them.
- The rate of accidental events due to machine background (Touscheck effect) must also be taken into account. With the new machine design, we expect an accidental event rate of 50 MHz, which means 5 MHz of events impinging on the LET detector. A time window of 5 ns will reduce the accidental rate by a factor 40. Further background rejection will be obtained by cutting on the deposited energy.

By the above-mentioned requirements we can impose some technological costraints to our detector:

- It must be made by high-Z material, in order to place a detector with a lenght of several X_0 so to minimize shower leakage,
- If crystals are used, they should have a high light yield, and a fast emission, in order to get the desired timing and energy capabilities,
- Photodetectors must be thin, radiation tolerant, with high gain and insensitive to magnetic fields.

Several suitable choices are offered by the most recent scintillating crystals and photodetectors that can in principle satisfy the above specified requirements. For instance, both the Lead Tungstate ($PbWO_4$) and the new Cerium doped Lutetium Yttrium Orthosilicate (LYSO) crystal scintillators can be considered, coupled to both Avalanche Photodiodes (APD) and Silicon Photomultipliers (SiPM) photodetectors.

All these new technological solutions have been investigated and tested in deep, in order to find the ones best fitting the LET requirements. Details about technical specifications and experimental tests of these new devices will be discussed in the following.

4.1 Detector simulation

The small available space for the LET, together with financial costraints, makes it neccessary to carefully choose the dimension of the active part of the detector in order to maximize the acceptance to e^+e^- while minimizing the shower leakage. In order to do that, extensive MonteCarlo simulations, made with the GEANT4 package, have been used to evaluate the expected energy and time resolution with different geometric options for the final design. A full simulation of the LET active volume has been carried out considering both LYSO and $PbWO_4$ crystals; the simulated beam trajectories have been used to exactly determine the detector response to the expected off-momentum particles. By changing detector dimensions and type of scintillator, we found that the best choice for the dimensions of each of the two LET detectors is 7.5x6x12 cm^3 (x, y, z). Fig. 26 shows the drawings of one of these LET detectors in place along the beam line. Each detector consists of 20 crystals, pointing to the average direction of the off-energy particles, i.e. 11 degrees with respect to the z axis, centered on the horizontal plane. With this design, the energy resolution is 12% for the $PbWO_4$ and 7% for the LYSO. Distributions of the energy deposits for the two options are shown in Fig. 36.

4.2 Experimental considerations

In the following we first discuss the possible options available for the detector choice. We then show the test performed with single crystals at electron test beams and summarize the status for the realization and test of a complete prototype. We finally recall the status of the test beam simulation and draw our conclusions on the detector choice.

4.2.1 Technology: crystals and photosensors

The discussion of the previous section indicates that the crystals needed for the Low Energy Tagger (LET) have to be very dense, fast, not igroscopic and with a reasonably high light

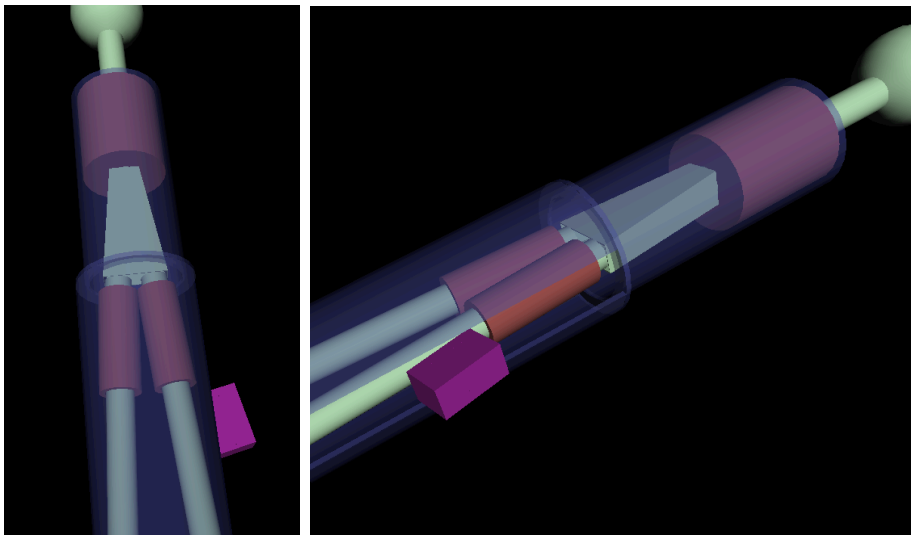

Figure 26: Top view (left) and side view (right) of one LET detector (violet box) on the DAΦNE beam-lines. The shaded surface is the mechanical support for LET and QCALT detectors.

Crystal	ρ (g/cm^3)	X_0 (cm)	n	R_m (cm)	Peak(nm)	photon yield	τ (ns)
$PbWO_4$	8.3	0.89	2.2	2.0	420	150/MeV	10
LYSO	7.4	1.14	1.8	2.1	420	32000/MeV	40

Table 3: Main characteristics of the two crystals under examination

output. Therefore we have selected the $PbWO_4$ and the LYSO crystals as possible candidates. In Tab. 3, we report the main properties of these crystals.

The LET detector is placed inside KLOE where an axial magnetic field of 0.52 T exists which forces the usage silicon based photodetectors (SPD). The new generation of SPD are divided in two large categories: the APD (Avalanche Photo Detectors) and the SiPM (Silicon Photo Multipliers). For the APD we specifically considered only the Hamamatsu S8664-55. The S8664-55 works in proportional mode, needs a bias voltage, Vb, of 370-410 V, has fast timing characteristics and has a very high quantum efficiency ϵ_q ($\sim$ 80%) in the blue region . The SiPM consists of an array of Silicon Photodetectors working on Geiger mode. It has a very large gain (0.4 to 4 10^6) , needs a bias voltage of $\sim$ 20 or 70 V which has to be set with high precision and stability ($<$ 20 mV).

In the following we describe in more details the crystal candidates and the related photo-sensors.

The $PbWO_4$ + SiPM option

The $PbWO_4$ is the well known Lead tungstate used by the CMS experiment. It has the advantage to be a very dense crystal not igroscopic and with a fast emission time (τ = 10 ns). The main disadvantage of this crystal is the low photon yield. CMS [29] accepted crystals of transverse and longitudinal dimensions ($2 \times 2 \times 2\text{cm}^3$) when a light yield greater than 8

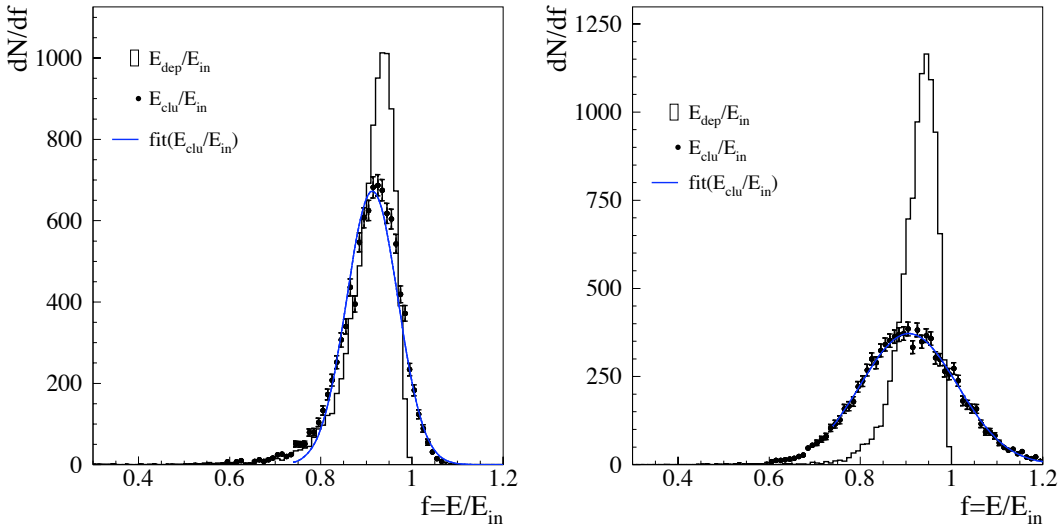

Figure 27: Deposited and detected energy in one LET detector, averaged over the impinging off-energy beam particles. Each plot shows for LYSO (left) and $PbWO_4$ (right) the fraction of deposited energy (solid) and detected energy (dots) over the impinging energy. To evaluate the detected energy distributions, 0.5 p.e. for $PbWO_4$ and 3.5 p.e. for LYSO have been used. Notice that the deposited energy fraction is similar in both cases and equal to 91%.

p.e./MeV was detected by a standard PM ($\epsilon_q = 25$ %). This corresponds to a photon yield of $\sim 150\gamma$/MeV and a collection efficiency dominated by total reflection ($\epsilon_c = (1-\eta_f/\eta_r) = 28\%$). Another important effect on the light collection is the optical coupling between the crystal surface and PM. Usage of optical grease or optical glue is needed to match the one of the photosensor sensitive area.

Therefore, even at low energies (i.e. below 0.5 GeV), these crystals could provide good energy resolution when photodetectors of large collection area are available. CMS solution was to read out the crystal with two APD's of 5×5 mm^2 area, i.e. a reduction factor 1/8 with respect to the Philips PM. Scaling down also for the different quantum efficiency, CMS measured a light yield of $\sim 4 p.e.$/MeV. This could be enough for our detector. However the not excellent light yield and the low value of the APD gain are not enough to match the sensitivity range of the KLOE-ADC. Indeed, the charge related to a single p.e. is given by:

$$Q_{1e} = G_{APD} \times G_{amp} \times 1.6 \times 10^{-19} C = 300 \times 100 \times 1.6 \times 10^{-19} C \sim 5 \times 10^{-15} C = 5\ rmfC, \quad (6)$$

where we have assumed an APD gain of 300, followed by an amplification stage of 100. At the minimum energy of 120 MeV, and assuming 4 p.e./MeV the charge collected by the APDs would be around $400\times$ 5 fC = 2 pC. With a sensitivity of $\sim$ 100 fc/count these electrons would provide a total charge of 20 ADC counts.

We therefore explored the road to match $PbWO_4$ with SiPM of large area. At the moment we have only two candidates at reasonable cost: the Hamamatsu MPPC of 3×3 mm^2 and the matrix of sixteen elements of 3×3 mm^2 area from SensL (250-300 Euro, 1100 Euro respectively). A summary of their characteristics is reported in Tab. 4. Hamamatsu also started offering matrix of 16 MPPC but at a price also increased by a factor 16.

SPD	Area(mm^2)	Pixel	Vb	Gain (Vb)	Dark Noise (MHz)	PDE(420 nm)
APD	5×5	uniform	400	100-300	–	0.8
MPPC	3×3	900	70	2.4×10^6	3.5	0.7
MPPC	3×3	3600	70	7.5×10^5	3	0.5
MPPC	3×3	14400	70	2.75×10^5	1.5	0.3
SENSL	13×13	58240	30	1×10^6	xxx	0.2

Table 4: Main characteristics of the SPD candidates. PDE stays for Photon Detection Efficiency. The APD has a almost uniform sensitive area and works in proportional mode so that the PDE corresponds to quantum efficiency. The SiPM works in geiger mode and the sensitive area is composed by pixels. The PDE is therefore the product of quantum efficiency, fill factor and avalanche probability.

The MPPC are a solid choice. In ref. [30], we have tested and measured different samples of 1×1 mm^2 area and checked that their characteristics are in good agreement with Hamamatsu data-sheet. Moreover, the Electronic Department of LNF (SELF) has already developed preamplifiers and prototype high voltage boards to correctly amplify ($G_{amp} = 20$), set and regulate with high stability (< 20 mV) the bias voltage on this detector. First prototypes of these amplifiers have also been developed for the larger area MPPC and have been used for the experimental tests we report in the next sections.

The large area SiPM from SensL is reaching a mature stage. These devices are planned to be used for an *improved replica* of the KLOE calorimeter at the GlueX experiment at Jlab. However, at the moment we have received only one prototype with related electronics (of dimensions $7 \times 7 cm^2$) which exceeds our space contraints. This prototype has been used for testing a single crystal.

The light yield for the readout option through a 3×3 MPPC as to face two reduction factors with respect to APD's:

- the ratio of the sensitive areas $R_A = 9/50$,
- and the ratio of the average quantum efficiencies $R_\epsilon = 0.5/0.8$, where we have assumed to use an MPPC of 400×9 pixels,

thus resulting in an expectation of $\sim 4 \times R_A \times R_\epsilon$ p.e./MeV $= 4 * 9/50 * 0.5/0.8 = 0.5$ pe/MeV, or slightly higher if we use shorter crystals than CMS.

For the SENSL option, we expect to get a larger light yield than for the MPPC candidate, due to an increase of the sensitive area of a factor 16 and a reduction of only a factor three-four in the quantum efficiency. A light yield of ~ 2.5 pe/MeV is feasible.

The LYSO+APD and the LYSO+SiPM option

Another very interesting crystal is the LYSO or Lutetium Yttrium Orthosilicate, which matches most of the$PbWO_4$ qualities with a much larger light yield ($\times$ 300) and a slower time response ($\tau = 40$ ns). The LYSO has also a smaller refraction index w.r.t the $PbWO_4$ which corresponds to a higher light collection efficiency. However, it has the advantage to have a reduced temperature dependence on the light output ($-0.2\%/^\circ$C).

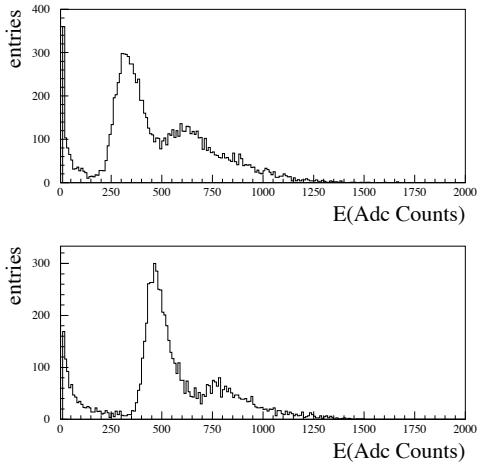

Figure 28: Distribution of energy respons in ADC counts for the horizontal (top plot) and vertical (bottom plot) scintillators.

Due to the high light yield, the option with APD readout is a valid solution since at the minimum value of 120 MeV the collected photoelectrons will be around $\sim$ 50.000 which correspond to $\sim$ 250 pC assuming the same amplification stage as in eq. 6. However APD's work with a bias voltage of 300-400 V and a dedicated board has to be built or bought for this purposes. To test this option we have built prototype for the amplifiers which were based on a Mar8+ with an amplification of 20 and a bandwith of 1 GhZ. The voltage output stage is limited at a peak of 1.5 V. The voltage bias to the APD was provided by a CAEN A1520P board (the same used in the CMS experiment) which provided a setting of the 400 V with a precision of x mV.

In the LYSO case, the readout option through SiPM is more difficult than for the $PbWO_4$ due to the saturation in the number of fired pixels. The only viable solution is to reduce the light yield to a reasonable value by means of optical filtering. To work in a linear region the maximum number of photoelectrons reaching the SiPM has to be $\sim$ 1/3 Npixels. The best option is therefore to use the MPPC with smaller size (25μm) which provides 11000 pixels A light yield of 4000 p.e. could still be in a linear region. We aim therefore to a detector with $\sim$ 10 p.e./MeV.

4.3 Experimental tests at BTF

Several tests have been performed at the Frascati BTF test-beam facility, in order to explore different technological options and geometrical designs of the LET calorimeters.

4.3.1 Early tests with single crystals

We have exposed different kinds of single crystals and photosensors at BTF with electron beams from 100 to 500 MeV, in order to study the different options we explored for scintillator and photosensor:

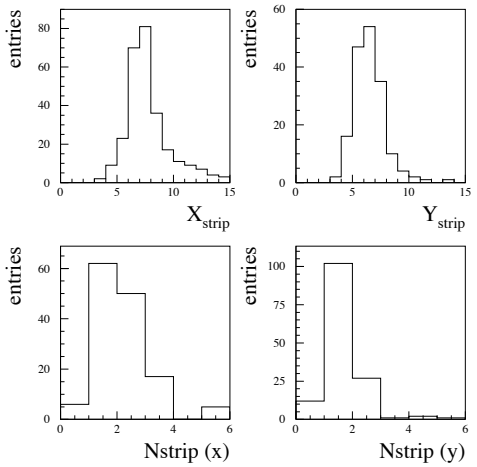

Figure 29: Distribution of scintillator strip fired on the X axis (top). Same plot ...

1. C1: a $PbWO_4$ crystal of $2 \times 2 \times 13$ cm^3 dimensions wrapped in Tyvek and optically connected by optical grease to a 3600 pixel MPPC. The MPPC was centered in the rear crystal face by means of a plastic holder.

2. C1bis: a $PbWO_4$ crystal of $1.5 \times 1.5 \times 13$ cm^3 dimensions readout by a 3600 pixel MPPC. The same crystal have also been tested with a prototype of the SensL photodetector.

3. C2: a LYSO crystal of $2 \times 2 \times 13$ cm^3 dimensions wrapped in Tyvek and with an optical filter inserted between the photodetector and the rear face. The filter consisted of differente layers (from 2 to 5) of 100 μm yellow plastic. Another test was done in a identical configuration with a smaller size crystal $2 \times 2 \times 10$ cm^3.

4. C3: $2 \times 2 \times 15$ cm^3 LYSO wrapped in tyvek and optically connected to a 5×5 o 10×10 mm^2 APD.

The crystals were positioned at the center of the beam axis with an area delimited by a cross of two BC408 scintillators of $1 \times 0.5 \times 5$ cm^3 dimensions, $f1, f2$, just in front of the crystal face. In most of the tests, the fingers were aligned in such a way that a beam spot of 0.5×0.5 cm^2 was defined. The beam was therefore crossing 2 cm of plastic scintillators (i.e. an average energy loss of ~ 4 MeV). In front of the fingers a beam position monitor, BPM, was also present; it consisted of sixteen horizontal and vertical scintillator strips readout by two Multi Anode PMs. Each strip was built by three 1 mm diameter scintillating fibers thus providing a sub-mm accuracy on the beam localization.

The trigger and readout scheme were the following:

- we triggered by using a gate synchronized with the beam injection;

- we used either the BTF or the KLOE-2 DAQ systems. In both cases, the trigger gate generated the ADC & TDC gates. In the KLOE case, we use one standard KLOE calorimeter ADC and TDC board, the new SDS and the CPU motorola;

- the gate was 300 ns long and the sensitivity of the boards was 35 (50) ps/count for the TDC nd 220 (100) fc/count for the ADC boards in the BTF (KLOE) daq.

The BTF beam allows to set the average number of electrons arriving to the detector. We show in Fig. 4.2.1, the example of the pulse height seen by one of the fingers. The inclusive distribution of BPMx, BPMy is also shown in Fig. 4.2.1.

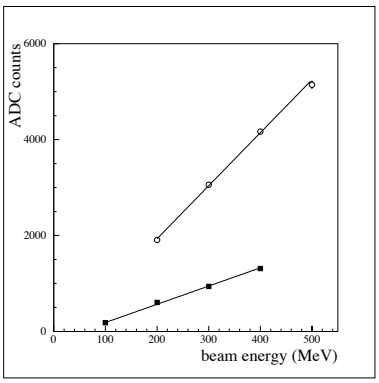

Figure 30: Linearity in energy response $PbWO_4$, LYSO

As an example of distribution, we show the energy response in ADC counts in Fig. **??** for the crystal 1 (top) and for the crystal 3 (bottom). The distributions are for 200 MeV (left plots) and 300 MeV (right plots) respectively. In these runs, we have used the BTF daq, in order to have a larger total integration charge (sensitivity of 220 fC/counts). Moreover, the LYSO crystal had the light output attenuated by means of two layers of yellow plastic filter. The signal was still too high for the ADC range but, since it was not saturating the amplifier, we used a simple resistive attenuator to reduce the signal by a factor of two. We have then analized few points at different energies, from 100 to 500 MeV, to check that no saturation occurred. Indeed this is proven by the linearity plot of Fig. 30. The LYSO and $PbWO_4$ crystals were connected to the same MPPC and operated at the nominal bias voltage Vb with a setting precision of 20 mV.

Assuming the SiPM gain at Vb as stated in their data-sheet, we estimated the $PbWO_4$ to have around 250 pe at 500 MeV. This corresponds to $\sim$ 0.5 pe/MeV. The LYSO crystal provides at least a factor of 3-4 larger light yield. Larger light output could be obtained by running with one layer only of optical filter and by using an MPPC with more pixels.

In Fig. 4.3.1, we show the distribution of time response, for crystal 1 (top) and crystal 3 (bottom), after having subtracted the jitter contribution of the trigger counters and corrected for time walk. As in the previous plot, the left (right) plots are for 200 (300) MeV respectively. A resolution of $\sim$ 1.1 (1.4) ns is observed for the crystal 1 (3) respectively. This already satisfies the LET requirement.

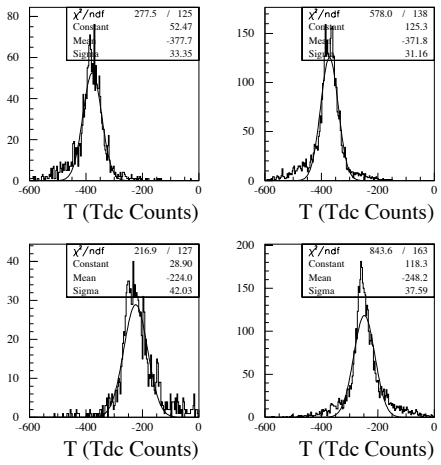

Figure 31: (top plots): distribution of time response for 200 MeV (left) and 300 MeV electrons on crystal 1. (Bottom plots): same distributions for crystal 3.

4.3.2 Prototypes for the LET detectors

In order to experimentally test the achievable energy and time resolutions of a system made of several crystals and to clarify the issues of assembly, calibration and stability of this kind of detector, we built two prototypes of crystal assemblies, to be tested under electron test beam and cosmic rays, of dimensions close to the ones of the final LET detectors. The first prototype had a transversal radius larger than 2 Moliere radius (R_m), and the longitudinal dimensions were constrained by budget requirement to be 13 cm.

This prototype was built on April 2009 and consists of an inner matrix with LYSO crystals readout by SiPM and an external matrix of $PbWO_4$ crystals readout by standard photomultipliers of 1,1/8" diameter. In Fig. 32.a, we show details of the matrix and of the assembly of the various components. In Fig. 32.b, we also show a picture taken during the mounting phase. The external holder takes the PMs in position at the center of the external crystals while allowing to press the box containing the SiPMs and their preamplifiers. The preamplifiers, designed and realized by the LNF electronic service, were connected on the SiPM backs.

In Fig. 37 we show the numbering scheme defined for the matrix and its composition. LYSO crystals were purchased by three different companies to compare their qualities.

A second prototype was built in October 2009, using the first batch of LYSO crystals purchased for the construction of the LET detectors. It was simpler than the first one, and of the same size and shape as one of the LET calorimeters to be built for data taking in KLOE-2. It consisted in 20 crystals, 15x15x120 mm^3 each, packed side-by-side to have a 5x4 crystals matrix structure. Each crystal was read-out by one Hamamatsu MPPC, 3x3 mm^2 active area, 14400 pixel each, coupled to custom front-end electronics again realized by LNF electronic service. This time an indirect coupling, i.e. via coaxial cable, was also tried between SiPM and Front-end with good results.

The front end electronics has been custom designed to satisfy the detector requirements and

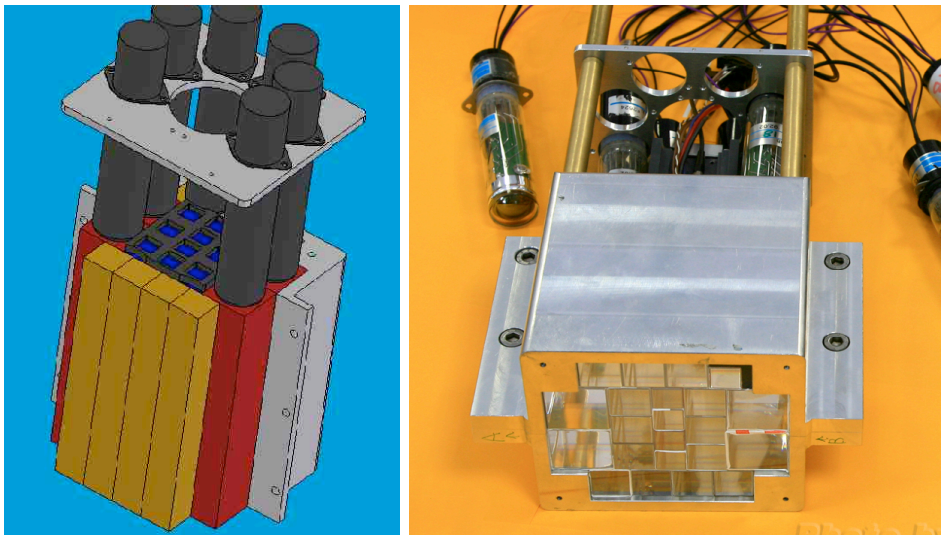

Figure 32: Mechanical drawings (left) and picture (right) of the prototype

to be compatible with the KLOE Electromagnetic Calorimeter (EmC) readout chain [31].

From the detector point of view, the main requirements are

- a very stable, low noise power supply for the SiPMs,
- a working voltage setting and monitor for each SiPM channel,
- a low noise, good linearity, low power consumption preamplifier,
- a good packing factor.

At the same time to be compatible with the EmC readout, the preamplifier output must be well matched with the input stage of the KLOE SDS (Splitter-Discriminator-Shaper) board.

To fulfil these specifications, a transimpedance preamplifier with embedded voltage regulator has been developed. The block diagram of the complete system is shown in fig. 33. The remote power module generates the main power supply for the on-board voltage regulator and allows setting and monitor of SiPM working voltage. A main DC voltage of 90 V with 100 mV of residual ripple can be distributed in parallel to several channels The working voltage of each SiPM was set via a programmable current sent to the correspondent voltage regulator, in the range 60 - 80 V. The use of a control current instead of a control voltage is needed to reach the required setting precision, solving the problem of the cables and contacts series resistance.

To obtain a very stable voltage minimizing the number of components, the voltage regulator used a new architecture based on a constant current source and a voltage reference source to control a variable impedance to regulate the input voltage.

In the first version of this front-end electronics, which has been used during the beam tests, a two transistors configuration with bootstrap technique has been adopted for the transimpedance preamplifier. Low noise microwave transistors with a transition frequency f_T of 5 GHz and a very low base spread resistance $r_{BB'}$ have been used to match the noise requirements ($2\mu V/\sqrt{Hz}$). Besides, the use of only two transistors operating at low collector current allows

to reach a power dissipation of 24 mW. The bootstrap technique is adopted to preserve the fast rising edge of the signal with a high detector capacitance.

The preamplifier with the embedded voltage regulator has been packed in a 10x20 mm2 board that can be mounted directly on the face of the LYSO crystal, on the SiPM pins.

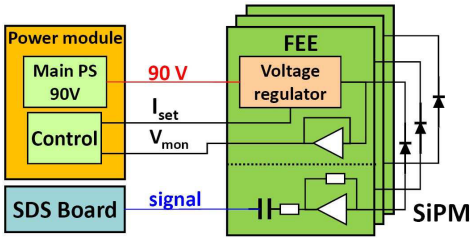

Figure 33: Block diagram of the LET front-end electronics

4.3.3 Test beam at BTF

Both prorotypes were tested at LNF BTF using a clone of the standard KLOE DAQ, in order to acquire data exactly with the same chain as in the experiment.

The first prototype was tested in May-June 2009, by exposing it to electrons of energy ranging from 150 to 500 MeV. The collected charge is shown in fig. 34. A linear response of LYSO+SiPM from 150 up to 500 MeV is achieved. This implies that less than 10^3 photoelectrons were collected at the maximum energy, which corresponds to $\sim$2 photoelectrons/MeV, consistently with what expected from the hardware setup. Results for the energy resolution are shown in fig. 35. The stochastic term is $2.8\%/\sqrt{E(GeV)}$, that is consistent with the $\sim$2 photoelectrons/MeV expected. The noise term was evaluated from the pedestals of the electronic channels, and contributes with 0.7%/E to energy resolution. Some additional noise due to test beam setup, brings the total noise contribution to 1.2%/E. A constant term of $\sim$4% is fully dominated by leakage, due to the shape of the prototype.

The second prototype was exposed to electrons of 100 to 450 MeV, and only 14 over 20 crystals were read-out. The best energy resolution and linearity were obtained with the cable-

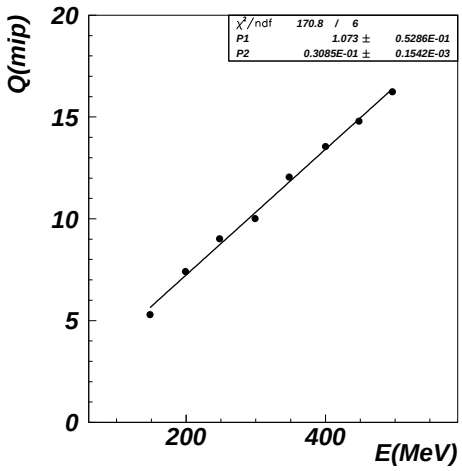

Figure 34: Energy response in minimum-ionizing particles' units for the crystal matrix, with respect to beam energy, for LYSO crystals only

coupling of SiPMs to front-end electronics . A contribution to the energy resolution came from the beam energy spread, which was higher than expected, and from the lateral leakage due to the unread-out crystals. We also tried to move the beam across the cracks between adjacent crystals, measuring no dead-zone effect.

This last test-beam validated the cable-coupling option, which was also supported by pervious laboratory test made with LED pulses.

4.4 Detector simulation

4.4.1 Simulation of the prototype

In order to understand in detail the signals observed in the crystal and to estrapolate to the full matrix, we have simulated the first prototype with Geant4, by creating two different volumes for the inner matrix, one made of $PbWO_4$ and the other one of LYSO. The external matrix was simulated with $PbWO_4$ crystals + PM.

For each crystal we have simulated a dead space of 100 μm of mylar and activated the optical transportation of photons inside the scintillating material. Photodetector simulation consists of a sensitive area with 100% efficiency. The correct emission curve both in frequency and time have been inserted for the different scintillators. An attenuation length of 100 cm is also assumed.

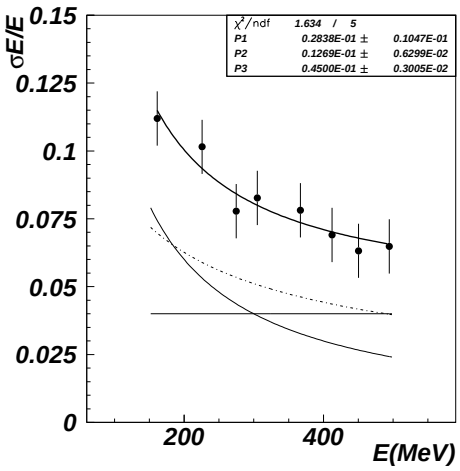

Figure 35: Energy resolution for the crystal matrix, as a function of the beam energy, obtained by summing up LYSO crystals only. Individual contributions from stochastic term (solid), noise (dotted) and constant term (horizontal dotted) are shown below the fit data.

4.4.2 Simulation of the final detector

The small available space for the LET makes it necessary to carefully choose the dimension of the active part of the detector to maximize the acceptance to e^+e^- while minimizing the shower leakage. In order to do that, extensive Monte Carlo simulations, made with the GEANT4 simulation package, have been used to evaluate the expected energy and time resolution with different geometric options for the final design. Simulations of LYSO and $PbWO_4$ crystals energy response allow us to evaluate the best fitting properties for the LET. A full simulation of the LET active volume and beam trajectories is used to determine the detector response to the expected off-momentum particles. By changing the simulated detector dimensions we find the best compromise between available space and energy resolution. Each detector will consist of crystals pointing to the average direction of the off-energy particles, i.e. 11 degrees with respect to the z axis, centered on the horizontal plane. Distributions of the energy deposits, for PbWO and LYSO crystals, are shown by solid line in fig. 36 for a 60x80x130 mm^3 detector.

4.5 Final considerations and cost estimates

From what we learned by the experimental test and the Monte Carlo simulation, and considering the cost of the possible options, we propose to build the LET detector using LYSO crystals coupled with SiPM photodetectors. The reasons for this choice are the followings:

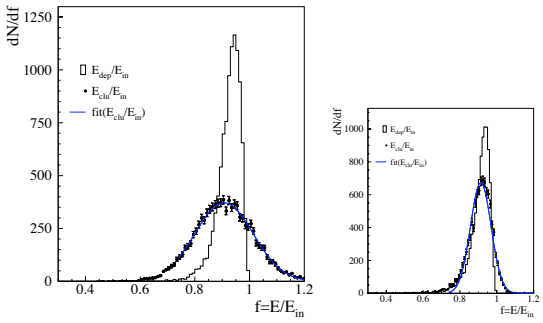

Figure 36: Deposited and reconstructed energy in one LET detector, averaged over the impinging off-energy beam particles. Each plot shows for LYSO (left) and $PbWO_4$ (right) the fraction of deposited energy (solid) and reconstructed energy (dots) over the impinging energy. To evaluate the reconstructed energy distributions, 0.5 p.e. for $PbWO_4$ and 3.5 p.e. for LYSO have been used. Notice that the deposited energy fraction is similar in both cases and equal to 91%.

- $PbWO_4$ crystals, even though having slightly shorter radiation length and smaller Moliere radius, have a light yield much smaller than the one of LYSO which has been measured experimentally by the number of photoelectrons collected on the photosensor. With a light yield of 0.5-1 photoelectrons per MeV, the slightly better containment achievable with $PbWO_4$ cannot be exploited to the overall energy and time resolution. LYSO can instead reach much better performances, thus fulfilling the requirements for the LET detector. During tests with SiPMs, the light yield of LYSO crystals had to be reduced by optical attenuators, in order to stay within the maximum number of photoelectrons allowed on the SiPMs presently in our hands. This loss in light output dynamics can be recovered, with an improvement in energy and time resolution, by using SiPMs with a higher number of pixels -already available on the market - . In addition, the light yield of $PbWO_4$ crystals has a temperature dependance of about $-3\%/°C$, which makes its use critical without a thermally stabilized vessel.

- SiPMs, with respect to APDs, have a lower bias voltage, and front-end electronics have already been developed and tested at LNF. This electronics can be easily modified with a different amplification stage. For these reasons, even though APDs could be a viable option coupled with LYSO for what concerns the light output, SIPMs have a more solid possibility to be successfully implemented in a final design within a short time. This issue also affects the cost of the LET realization: the R&D efforts already done for SiPM power supply and readout electronics makes this option cheaper than the APD one, for which the electronics should be designed and tested almost from scratch.

The proposed design consists of two identical stations, each one made by 12 LYSO crystals of 2x2x13 cm^3, for a total dimension of 6x8x13 cm^3 per station. Each crystal is equipped with a 3x3 mm^2 sensitive area SiPM, for a total of 24 power supply and readout channels for both the stations. The detailed costs are reported in table 5.

The signals from the amplifiers will be transported by cables to the backplane of the KLOE SDS boards. The readout will be carried out with one KLOE calorimeter ADC and TDC board.

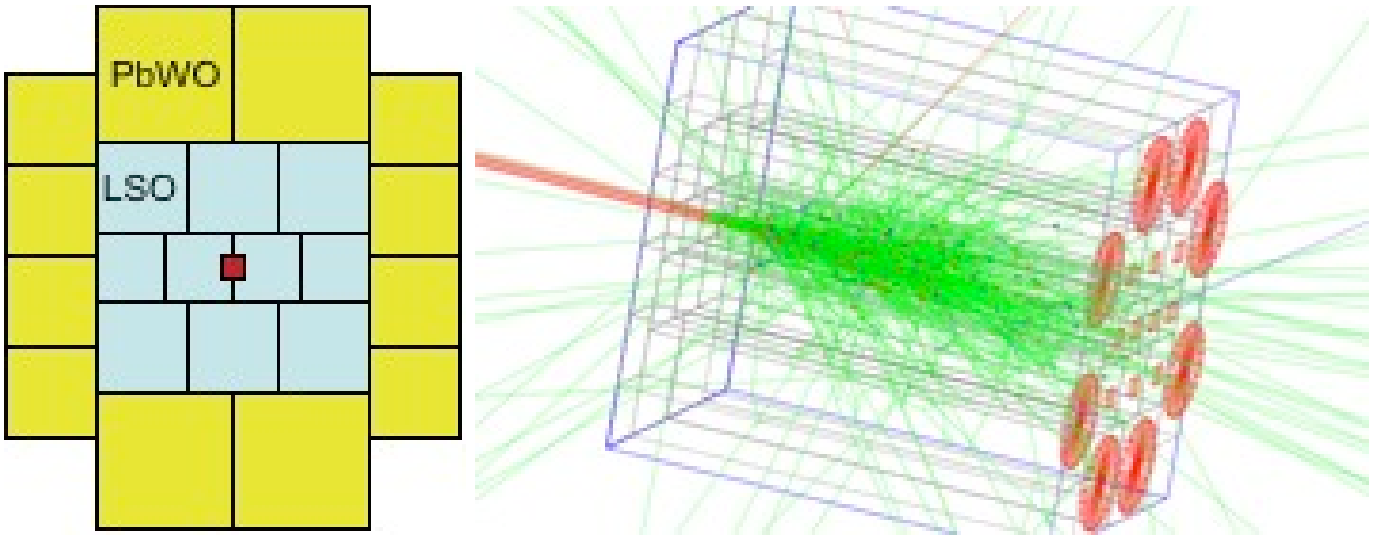

Figure 37: View of the simulated electron beam impinging on the crystal matrix

A final board for voltage setting with remote control will be developed in the next months for the 2010 run.

Mechanical considerations on the mounting are being addressed. No problems are foreseen on this point due to the small size and weight of the object. The insertion job will be coordinated with the operation of building the beam-pipe aluminum support and the machine background screens.

item	cost (Keuro)
24 LYSO crystals of 2x2x13 cm^3	35
24 Hamamatsu MPPC 3x3 mm^2	10
front-end electronics	10
high voltage supply	5
total	60

Table 5: Cost estimate for the LET detectors

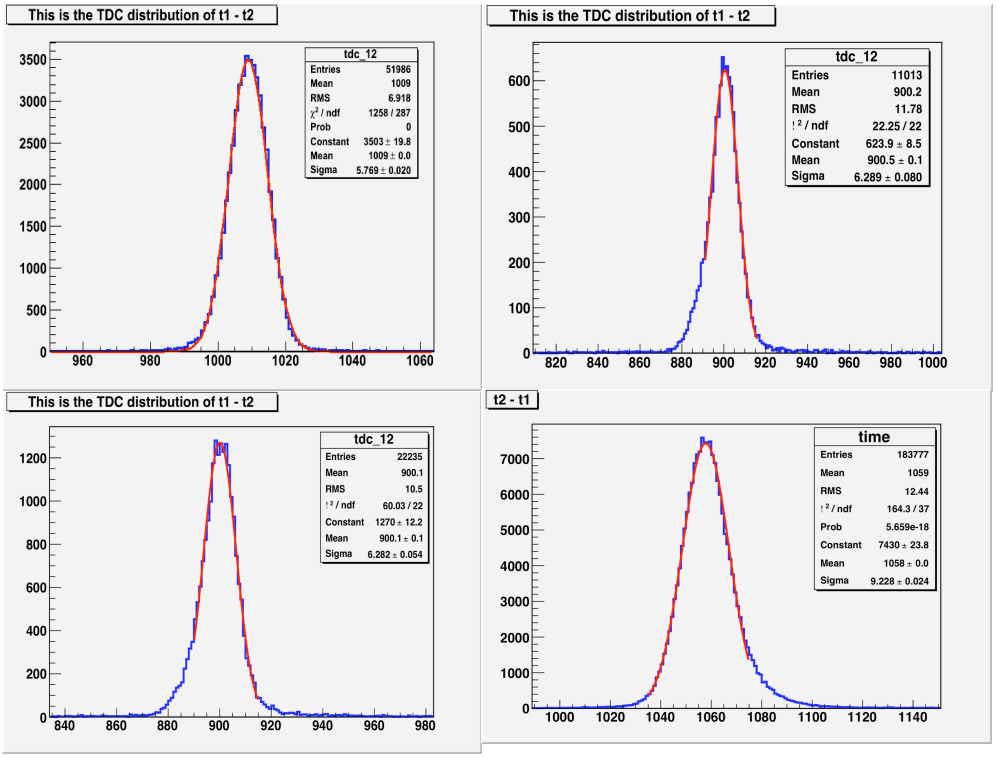

Figure 38: Results of the test performed at the BTF@LNF.

5 The HET tagger characteristics

The HET detector should provide a measurement of the displacement of the scattered leptons with respect to the nominal orbit. Therefore this detector should be inserted inside the machine lattice, as close as possible to the beam line. The possible access point is located after the dipole placed 11 m from the IP. The physical requirements are summarized as follows: good time resolution to disentangle each bunch coming with a period of $\sim$ 2.7 ns; capability to acquire data at a frequency of 368 MHz in order to permit event reconstruction with the KLOE apparatus; radiation hardness in order to stand 50 mm from the beam (a closer position would interfere with the proper functioning of the machine) for long term acquisition; and tiny size to allow the installation with the mechanical support inside the DAΦNE vacuum chamber.

The tagger detector consists of a set of scintillators arranged in two "stairs" and is constituted of 30 EJ-228 scintillators $3 \times 6 \times 3$ mm^3, which provide, in this geometry, a spatial resolution of 2 mm (corresponding to momentum resolution of 500 keV). Two additional $3 \times 6 \times 120$ mm^3 are used for coincidence.

The output light is collected by clear light guides coupled with Hamamatsu R9880U-110sel photomultipliers.

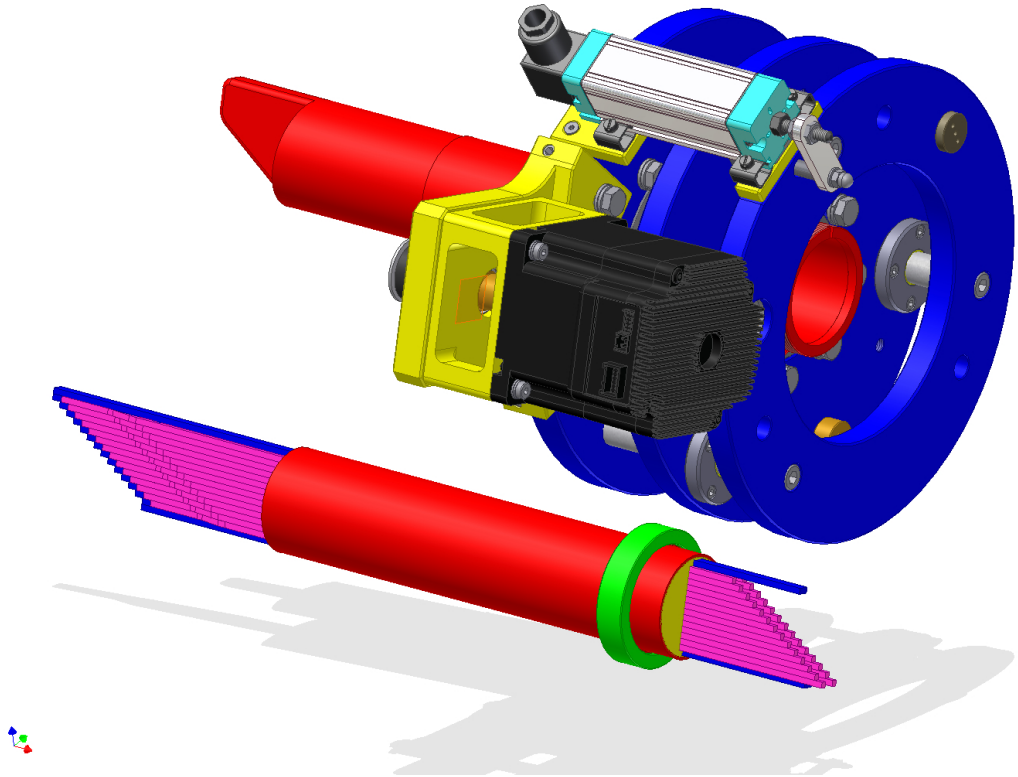

Figure 39: A rendering of the HET apparatus. Both the mechanical system (up) and the detector itself (down) are shown

In spring 2009, a series of tests has been performed at the Beam Test Facility (at Laboratori Nazionali di Frascati) in order to study the time performances of the detector. The time of flight of electrons have been measured with a HET prototype composed of only two modules (scintillator and photomultiplier). A time resolution of ∼300 ps has been obtained, the plots of the measurements are shown in figure 39.

To minimize the interference with the DAΦNE high vacuum system, the detector system will be installed inside a movable steel sleeve shaped box open to air in one side.

6 Mechanics

Flanges, box, and motors are ready. We are cleaning all the parts for vacuum and we are going to solder the vacuum chamber and install the engines.
Finally we will give the mechanical system to the vacuum experts for the final cleaning and test.
We are going to install the mechanical system on DAΦNE within the end of March 2010.

7 Slow Control

We have to monitor the efficiency of the PMTs and compensate (as much as possible) the ageing of the photocathode by increasing the high voltage supply. An automatic system, controlled via Ethernet, is being developed.
The Slow Control system will be structured as follows:

- A pulsed LED controlled by a linear current generator (already tested successfully);
- 32 optical fibres to bring exactly the same light to the each PMTs;
- A 32 channels CAEN VME QDC to acquire the spectrum of every single PMT;
- A VME board with a PIC microcontroller to monitor the efficiency of the PMTs (with the procedure prevously described) and consequently change the HV supplied.

In case of serious damage of a PMT it can be easily replaced thanks to the mechanical structure that is being designed.

8 Frontend Electronics

The frontend board is designed. It is composed by

- A fast buffer: LMH6559;
- An Amplifier: LMH6703;
- Two voltage regulators: MC78LC00 and MIC5270;
- A thermometer TC1047A.

The frontend board will provide an analog signal to the Data Acquisition board which is embedding the discriminators (LMH7324). This part of the electronics chain has being tested yielding excellent results: the output signal has a rise time shorter than 0.5 ns.

9 Data Acquisition

The signals come from the HET detector, DAΦNE (fiducial) and KLOE (Trigger and ACQ logic); Acquisition logic (TDC) has been implemented inside the FPGA; A microcomputer, inside a Virtex5 FPGA, handles the communication with KLOE DAQ via the VME bus.
As the HET detector is placed far away from the IP, we need to keep track of the number beam bunches, i.e. we need to count them. Thus we must distinguish to consecutive bunches: we need a time resolution ¡ 1 ns; The input stage has been tested (4-phase DCM - 0.5ns); We are able to reach such a time resolution with 500 MHz clock using a DCM and several delay lines. The 8-phase DCM (0.25 ns) has been developed and is currently under test. The Linux OS for the Virtex5 is being configured and VME Drivers (provided by Roma3) are being adapted to fit Virtex5 board. The board itself is currently being designed, and will be built and tested in the next few months.

9.1 HET Cost Estimate

In the following table we report the cost estimate for the two HET detectors.

Item	cost (kEuro)
Mechanics	38
60 Plastic Scintillators	10
60 Hamamatsu MPPC 3x3 mm^2	25
HV supply + Cables	10
Front-End electronics	14
3 Virtex5	14
2 Motorola	8
Total	119

Table 6: Cost estimate for the HET detectors

10 Summary and Time schedule

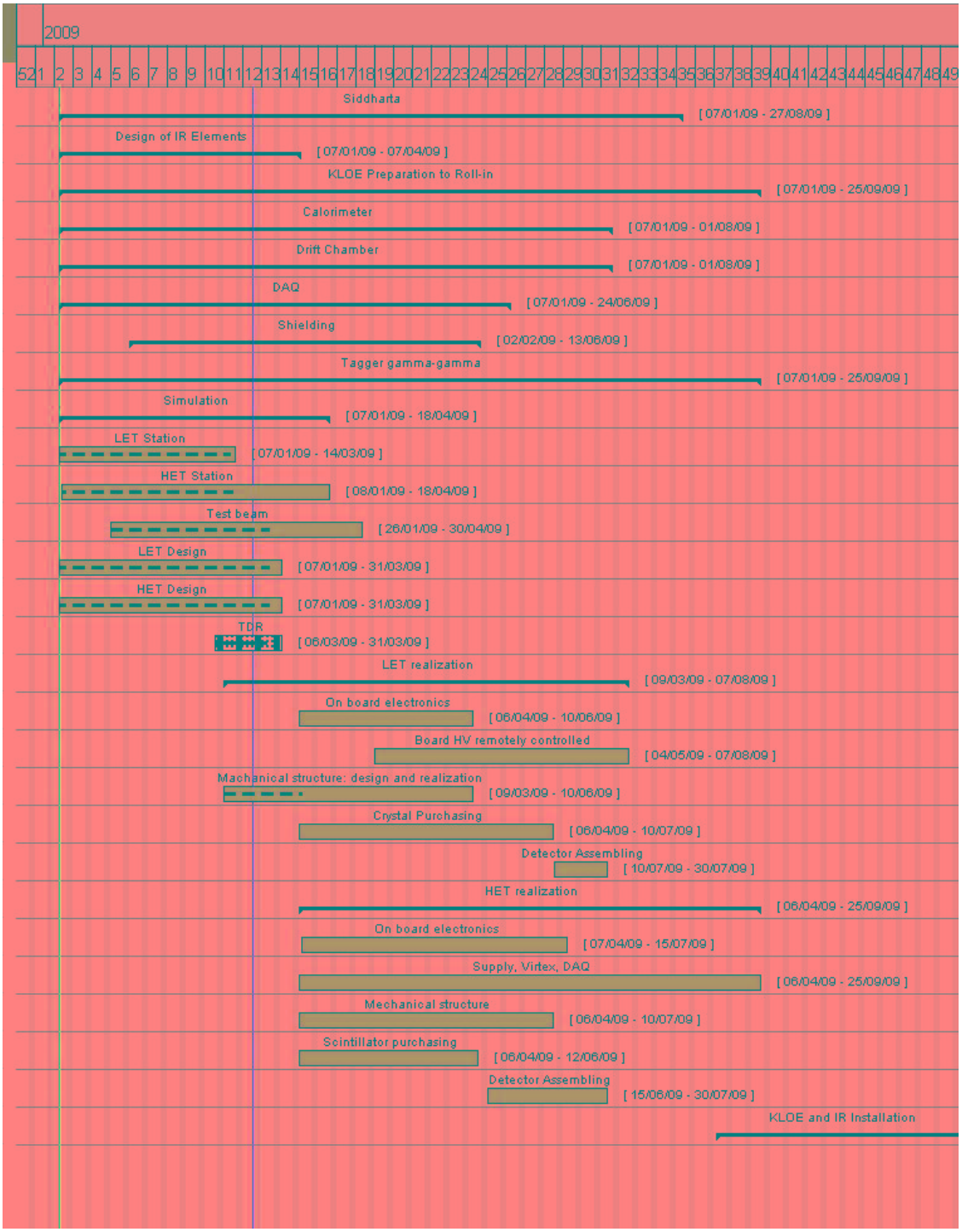

Figure 40: KLOE-2 schedule

References

[1] S. J. Brodsky, T. Kinoshita and H. Terazawa, Phys. Rev. Lett. **25**, 972 (1970).

[2] see the review by M. R. Pennington, [arXiv:hep-ph/0511146] and reference therein.

[3] H. Marsiske et al. (Crystal Ball Collab.), Phys. Rev. D **41**, 3324 (1990).

[4] G. Alexander et al., Nuovo Cimento **107A**, 837 (1994); F. Anulli et al., *The second DAΦNE Physics Handbook*, Vol. II, eds. L. Maiani, G. Pancheri, and N. Paver (1995), p. 607.

[5] I. Caprini, G. Colangelo and H. Leutwyler, [arXiv:hep-ph/0512364].

[6] E.M. Aitala (E791 Collab.), Phys. Rev. Lett. **86**,770 (2001).

[7] M. Ablikim et al. (BES Collab.), Phys. Lett. **B598**, 149 (2004).

[8] A. Deandrea and A.D. Polosa, Phys. Rev. Lett. **86**, 216 (2001); S. Gardner and U. Meissner, Phys. Rev. **D65**, 094004 (2002); I. Bigi, [arXiv:hep-ph/0601167].

[9] B. Aubert et al. (BaBar Collab.), Phys. Rev. Lett. **95**, 121802 (2005).

[10] F. Nguyen, F. Piccinini and A.D. Polosa, Eur. Phys. J. C**47**, 65 (2006).

[11] S. J. Brodsky, T. Kinoshita and H. Terazawa, Phys. Rev. D **4**, 1532 (1971).

[12] A. Bramon, R. Escribano and M. D. Scadron, Eur. Phys. J. C **7**, 271 (1999).

[13] E. Kou, Phys. Rev. D **63**, 054027 (2001) .

[14] F. Ambrosino et al. [KLOE Collaboration], Phys. Lett. B **648**, 267 (2007).

[15] F. Ambrosino et al., Eur. Phys. J. C**50**, 729 (2007).

[16] F. Jegerlehner and A. Nyffeler, "The Muon g-2", arXiv:0902.3360 [hep-ph].

[17] E. Abouzaid *et al.* [KTeV Collaboration], Phys. Rev. D **75** (2007) 012004

[18] A. E. Dorokhov, Nucl. Phys. Proc. Suppl. **181-182** (2008) 37.

[19] T. Oest et al. (JADE Collab.), Z. Phys. C **47**, 343 (1990).

[20] J. Gasser, M.A. Ivanov and M. Sainio, Nucl. Phys. **B728**, 31 (2005); see also S. Bellucci, J. Gasser and M. Sainio Nucl. Phys. **B423**, 80 (1994); erratum-ibid. **B431**, 413-414 (1994).

[21] M. R. Pennington, *The second DAΦNE Physics Handbook*, eds. L. Maiani, G. Pancheri, and N. Paver (1995), p. 531.

[22] A. Courau, SLAC - PUB - 3363 (1984).

[23] http://mad.web.cern.ch/mad

[24] http://www.pp.rhul.ac.uk/ malton/bdsim.

[25] J. Carter, I. Agapov, G. A. Blair and O. Dadoun, Pramana **69**, 1133 (2007).

[26] L. Quintieri et al., preprint LNF-09/03 (IR).

[27] S. Uehara, private communications; for details on TREPS see http::/belle.kek.jp/ uehara/treps-readme.html.

[28] A. Bartalini et al. Eur. Phys. J. A**26**, 399 (2005).

[29] L.M. Barone et al., Nucl. Instr. Meth. **A562**, 76-84 (2006)

[30] .....

[31] M.Adinolfi et al. [KLOE Collaboration], Nucl. Instr. Methods **A482**, 364-386 (2002).